DRAFT

ANALYSIS NOTE
Absolute Polarization Determination at RHIC in 2005

K.O. Eyser, I. Alekseev, A. Bazilevsky, A. Bravar, G. Bunce, S. Dhawan, R. Gill, W. Haeberli, H. Huang, Y. Makdisi, I. Nakagawa, A. Nass, H. Okada, E. Stephenson, D.N. Svirida, T. Wise, J. Wood, A. Zelenski

Collider-Accelerator Department
Brookhaven National Laboratory
Upton, NY 11973

Analysis Note
Absolute Polarization Determination at RHIC in 2005

K.O. Eyser, I. Alekseev, A. Bazilevsky, A. Bravar,
G. Bunce, S. Dhawan, R. Gill, W. Haeberli,
H. Huang, Y. Makdisi, I. Nakagawa, A. Nass,
H. Okada, E. Stephenson, D.N. Svirida, T. Wise,
J. Wood, and A. Zelenski

May 22, 2007

Contents

1 Introduction

The knowledge of beam polarizations in RHIC is based on two crucial premises. Fast measurements have to be carried out at several times during a fill, which include injection energy and regular intervals at storage energy. These measurements only need a relative comparison for polarization development and polarization preservation in the accelerator. The physics program, on the other hand, relies on the knowledge of the absolute value of the polarization.

In order to comply with these requirements, two different devices have been installed into the accelerator. A hydrogen jet target polarimeter provides an absolute normalization for the polarization. Precise measurements with sufficient statistical accuracy cover many fills and usually have to run over several days for a single beam. Two carbon target polarimeters (pC) with fiber targets can determine the beam polarization for each beam within a minute or less. Certain theoretical and experimental challenges prevent these polarimeters from measuring the absolute polarization from the very beginning.

For the RHIC spin physics program, the accuracy of the beam polarization measurement $\left(\frac{\Delta P}{P}\right)_{beam}$ has the goal of:

$$\left(\frac{\Delta P}{P}\right)_{beam} \leq 5\%. \tag{1}$$

Our approach is to measure the beam polarization directly with the jet, alternately with the blue and yellow beams, and to use these measurements also to calibrate the pC polarimeters. We then use the pC polarimeters to determine the beam polarization for each beam for the periods when the jet did not measure the polarization directly for that beam.

In the following, this analysis note describes the measurements with the jet polarimeter in the RHIC 2005 run. In order to provide the necessary normalization, different asymmetry calculations are presented and compared. A detailed study of background and systematic errors show that the polarization measurements are close to the set goal.

2 Setup

The hydrogen jet target provides an absolute polarization normalization for the RHIC proton beams. It detects recoil protons from elastic scattering at very small momentum transfer. Interference of Coulomb and nuclear contributions (CNI) results in a maximum of the analyzing power $A_N \approx 4 - 5\%$, which was predicted from the interference of the electromagnetic spin flip amplitude that generates the proton anomalous magnetic moment, and the hadronic spin non-flip amplitude that is obtained from the p+p total cross section. This expected asymmetry, with the large cross section for small angle scattering, therefore led to a predicted large figure of merit for using CNI scattering to measure the RHIC beam polarization. This was confirmed in the 2004 run [1]. Furthermore, the use of elastic scattering allows an elegant approach to transfer knowledge of the polarization of the proton jet target through measurement of only the recoil proton asymmetry to determine the beam polarization.

The jet polarimeter was commissioned in 2004 and was used with the blue RHIC beam only. In 2005 the detectors were shifted to be able to measure with both beams. Measurements were taken with both beams simultaneously on the jet target, initially, in 2005. To do this, the beams were separated vertically to avoid collision background, and to avoid beam-beam interactions which can cause increased beam emittance and reduce the RHIC luminosity. However, higher backgrounds and reduced detector acceptance from the displaced beams led to our measuring the polarization of the beams separately for the rest of 2005.

2.1 Jet Target & Detectors

The jet polarimeter uses a polarized atomic hydrogen target [2]. A molecular hydrogen beam is dissociated and focussed through a cooled nozzle, after which it passes an inhomogeneous sextupole magnetic field and a radio frequency transition unit. As for the Stern-Gerlach experiment, the magnetic field leads to a hyperfine splitting of atomic hydrogen. Due to the larger electron magnetic moment, only one electron spin state is focussed in the inhomogeneous field, the other state is defocussed or sorted out. The electron spin polarized beam passes the transition unit, where an electromagnetic wave induces a transition of one of the hyperfine states into another. This transition depends on the frequency (energy) of the electromagnetic wave and
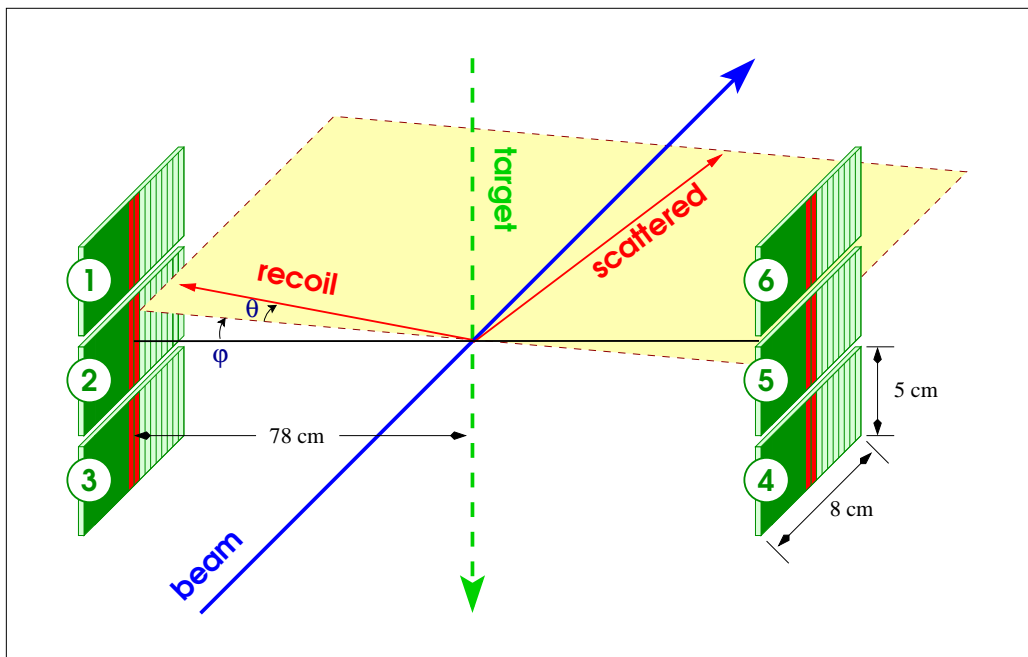
Figure 1: Setup of the jet target and the six detectors (labeled 1 through 6) around the interaction region with the RHIC beam (blue). The scattering plane (yellow) is rotated by φ with regards to the accelerator plane. Shown for the blue beam passing through the center of the jet target; the yellow beam, not shown, would be displaced 1 cm horizontally and vertically. Not to scale.

transfers the electron polarization into a proton polarization either parallel or antiparallel to the magnetic holding field.

The jet target polarization is constantly measured with a Breit-Rabi polarimeter after the atoms pass through the interaction region. The target polarization is extremely stable in time and measured every six seconds to much less than 1% statistical uncertainty. The atomic polarization is $P_{atomic} = 96\%$. Recombination and other background lowers the effective proton target polarization to $P_{eff} = (92.4 \pm 1.8)\%$. (This estimate of the molecular background and effective hydrogen polarization is based on 2004.)

Figure 1 shows the detector setup for 2005.

Figure 1 shows the detector geometry for 2005. The silicon strip detector characteristics are described in [3], with the detectors and geometry for the

2004 run. In 2004 the detectors were mounted to only measure forward scattering from the blue beam. The detectors and geometry were changed for the 2005 run, and set up to measure scattering from both blue and yellow beams by centering the detectors at 90 degrees from the beams, left and right. All six detectors were Hamamatsu type, pp2pp design, active area 50 mm vertically and arranged in 18 channels, each 4.44 mm wide (by connecting 40 individual strips to form one channel, referred to either as channel or strip in this note). Eight downstream channels from each end were read out for each detector, providing coverage for scattering from both beams. The two central channels on each detector were not read out. The active area therefore was from 4.44 mm from the target center plane (θ=0 in Fig. 1) to 40.0 mm for scattering from each beam, in polar angle θ. However, the geometry of scattering to left and right is not symmetric due to the vertical magnetic holding field. This field, which has a net field integral of 0 due to an opposing coil arrangement, displaces the recoils by about 1/2 channel for scattering to left and right, one side displaced upstream and one side downstream. The detectors were 78 cm from the collision point, staggered by 1 cm steps for mounting purposes, and nearly adjacent to each other in the azimuthal angle φ (the azimuthal angle subtended was about $\pm 6°$ from horizontal for the three detectors).

2.2   Data Acquisition

Each silicon strip had its own electronic chain, including preamp, amplifier, shaper, and waveform digitizer (WFD) channel. Additional WFD channels were built for the 2005 run to separate the jet measurement WFDs from the pC measurement WFDs (the WFD channels had been shared previously). An important difference in 2005 was the use of the 120 bunch mode in RHIC, where beam bunches were separated by 106 ns, rather than the 212 ns separation of the 60 bunch mode used in 2004 and part of 2005. The jet waveform shape had a rise time (10% to 90% of pulse maximum) of 14 ns and a half width of 31 ns, in 2005 (changed from 2004). With the bunch separation of 106 ns, and the event gates set to accept the pulse within the bunch crossing time, the tail of the waveform was cut off for later arriving pulses (lower energy recoils) in the 120 bunch mode. This was not the case for the 60 bunch mode running. However, the pulse maximum and time based on quarter pulse maximum were not affected. The data were analyzed in separate groups, according to whether 60 or 120 bunch mode setups were used, in any

case.

2.3   Data Set

In 2005, data sets, as discussed above, included a first run with both beams, displaced vertically on the jet target, and subsequent runs alternating between centering either the yellow or blue beam on the jet target, with the other beam displaced horizontally and vertically by about 1 cm. At this position the displaced beam was shadowed from the detectors by the rf shield that is a part of the target setup [2]. Furthermore, initial RHIC running used the 60 bunch mode, followed by increasing the number of bunches in a 120 bunch mode pattern. Over the course of a few weeks, the number of bunches, using the 120 bunch mode, was increased to 111. The polarimeter data acquisition system was changed to a 120-bunch mode setup before the first fill when directly adjacent filled bunches was begun. Both the *60-* and the *120-bunch mode* setups were used for polarization measurements of the blue and the yellow beams. The data set can therefore be divided into five different subsets, see table 1. Between data set 2 and data set 3 (actually on 4 May 2005), an access was made to the jet and the recoil arms were realigned. This reduced a left-right acceptance asymmetry that is noticeable for higher recoil energy in data sets 0 and 2. Collimators were also added to the recoil arms to reduce any background in the recoil detectors from scattering from upstream or downstream of the interaction region (this had little effect). Measurements of blue and yellow polarizations in *120-bunch mode* were carried out repeatedly and alternatingly, compare the overlapping periods in table 1. The number of events refers to the yields within all particle identification cuts of elastic proton-proton scattering and are used for the asymmetry calculations.

2.4   ADC Calibrations

The energy calibration of the ADC signals is done with α-sources that were mounted on each detector arm, with Americium (^{241}Am) used for the detectors on both sides of the beam, and Gadolinium (^{148}Gd) used for the detectors on the south side (to beam right for the blue beam direction). In 2005, the sources were blocked during data taking. Americium-241 decays mainly through 5.486 MeV (85%) and 5.443 MeV (13%) α-particles. Gadolinium-150 decays completely via 3.183 MeV α-particles.

Table 1: Data sets for the 2005 RHIC run. The number of events refers to the identified, elastically scattered proton-proton scattering events, summing over 2 strips per energy bin. Not shown is the commissioning period for 205 GeV/c.

data set	from	until	beam	mode	runs	events
0	04/21	04/29	both	60-bunch	47	$0.8 \cdot 10^6$
2	04/26	05/03	yellow	60-bunch	32	$0.7 \cdot 10^6$
3	05/03	06/24	yellow	120-bunch	127	$3.7 \cdot 10^6$
4	05/17	05/20	blue	60-bunch	19	$0.5 \cdot 10^6$
5	05/20	06/21	blue	120-bunch	71	$2.9 \cdot 10^6$

Figure 2 shows an example of a calibration spectrum from a north side silicon strip (red curve). The high peak at large ADC counts shows the 5.483-6 MeV α-particles from the Americium source. There is a small extension to lower energies that might account for lower energy decay modes. For the Gadolinium, there are clearly two peaks visible at about half of the ADC of the Americium. The double peak originates from differences in the thickness of the entrance window above the active area of the silicon strips, i.e. about half of the area is covered with aluminum electrodes that add to the entrance window. It is, however, not really clear why the double peak is not seen for the Americium signal.[1]

Figures 3 and 4 summarize the calibration spectra for all 96 silicon strips, grouped into the six detector pads from top to bottom on the right and left sides. Although there are differences between the single strips, overall the energy calibration is in the same range for all strips.

The signals in the spectra are fitted with gaussians (black curves in figure 2). Therefore, first the peak positions are searched as local maxima, allowing for one to four peaks above 150 entries.[2] The gaussian fit is then limited to five or six bins around the found peak position. Usually, the local maximum finding and fitting works well. Only the two Gadolinium peaks are in some cases to close together, and only one of the fits converges on top of the higher

---

[1]Ron Gill has carried out measurements in December 2006 that show how the double peak develops with increasing voltage. For 2005, a bias of 180 volts was used.

[2]The minimum of 150 entries for a peak removes random peaks from noise or background, e.g. the small local maximum below the Gadolinium signals in figure 2.
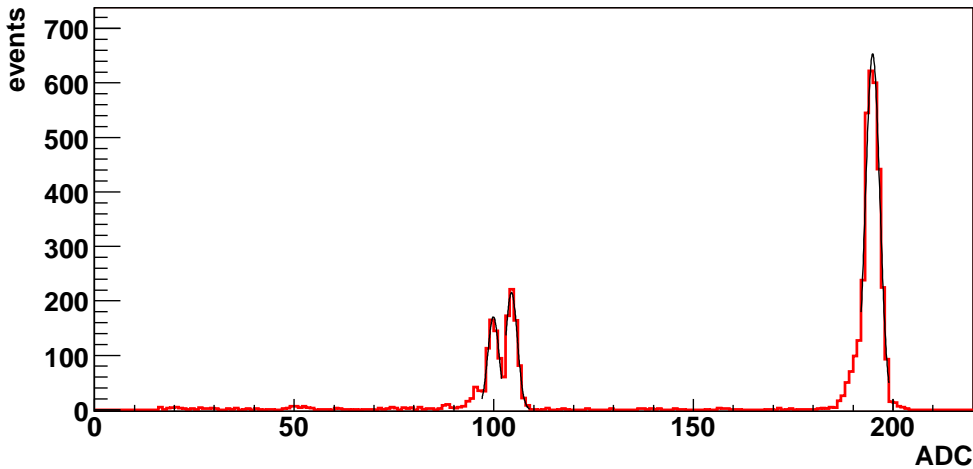
Figure 2: A typical event spectrum with Am and Gd signals in a single strip.

signal.

Fit results and the agreement between fit and local maxima can be seen in figure 5. Black circles show the Americium signal, red squares and blue triangles are the two Gd-signals. There are two cases, in which two peaks for the Americium source can be seen. And in some cases the fit does not really sit well on top of a local maximum and the width (error bar) is large. The lower part of the figure shows the differences between the fit and the underlying local maxima. Error bars represent one sigma of the gaussians. Most of the fits are within one ADC count of the local maximum and the difference always smaller than its width.

The energy calibration is calculated from the fit results. The double peaks of signals lead to a decreased energy resolution. On the other hand, double peaks for both signals would be a good check of the linearity of the detectors. It is:

$$E_{meas,i} = T_{kin} - \Delta E_i = c_i \cdot ADC_i \tag{2}$$

with the measured energy E_{meas}, the energy of the α-particles T_{kin}, the energy loss in the entrance window ΔE, and the ADC counts ADC. c is the ADC-to-energy calibration constant for each strip i.

Now, for two different α-energies and two different entrance window thicknesses, this reads:

$$E_{Am,meas,1,i} = 5.486 \text{ MeV} - \Delta E_{Am,1,i} = c_i \cdot ADC_{Am,1,i}$$
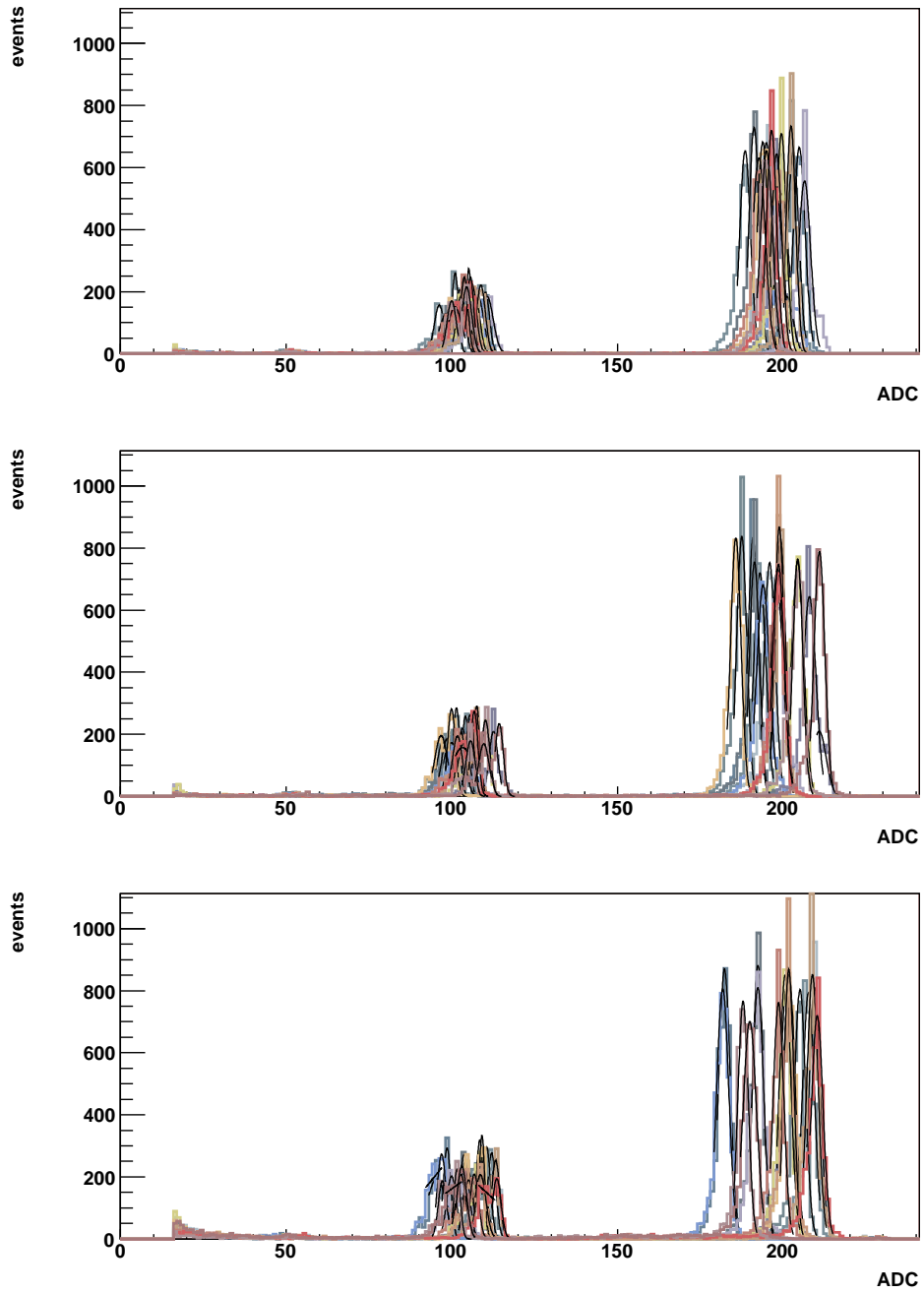
8

Figure 3: Calibration spectra for all Silicon strips with Am and Gd peaks. The spectra are separated for three detectors (top to bottom) on one side of the polarimeter (the south side detectors 4.5.6).
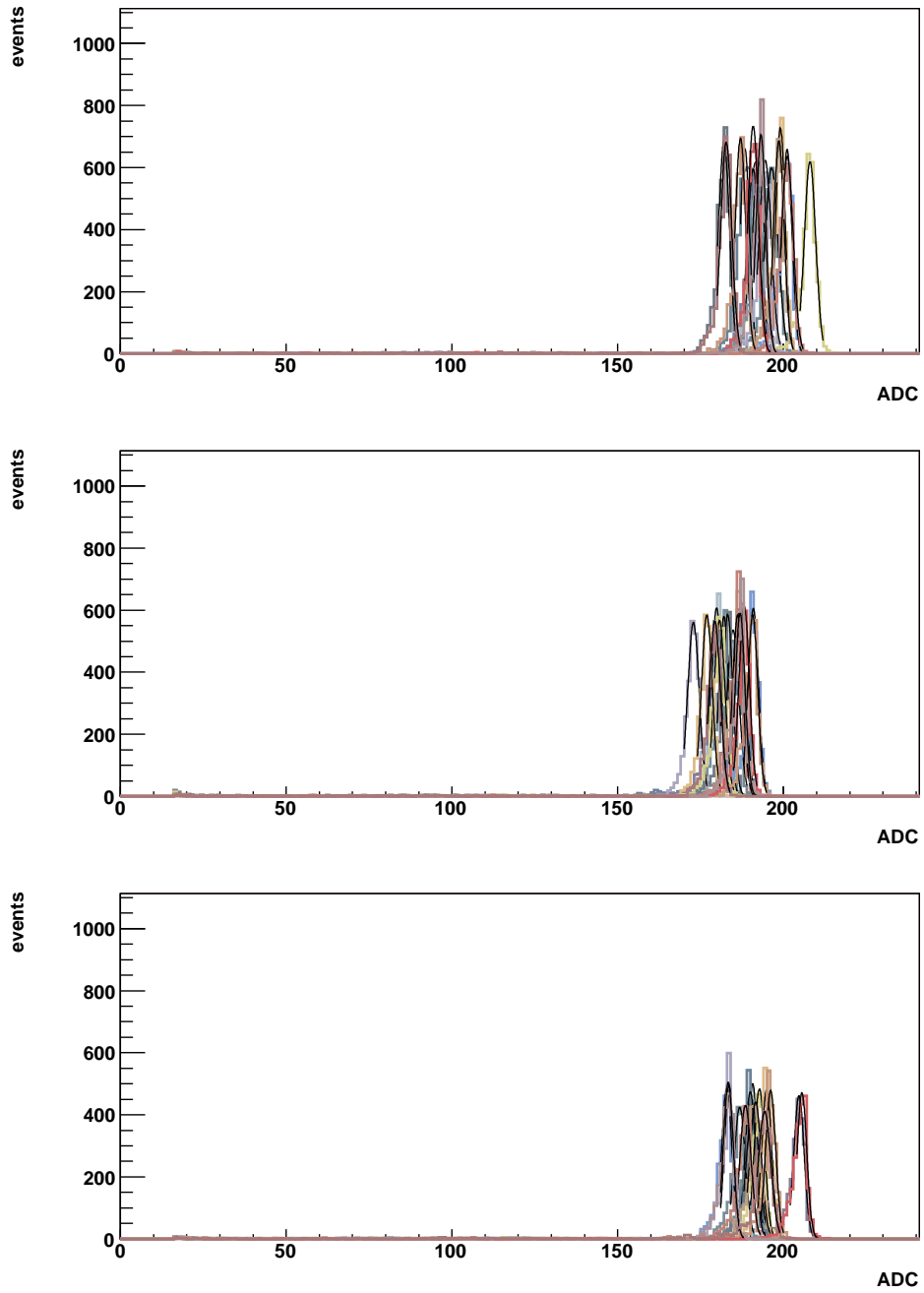
Figure 4: Calibration spectra for all Silicon strip with only Am peaks. The spectra are separated for three detectors (top to bottom) on one side of the polarimeter (the north side detectors 1,2,3).
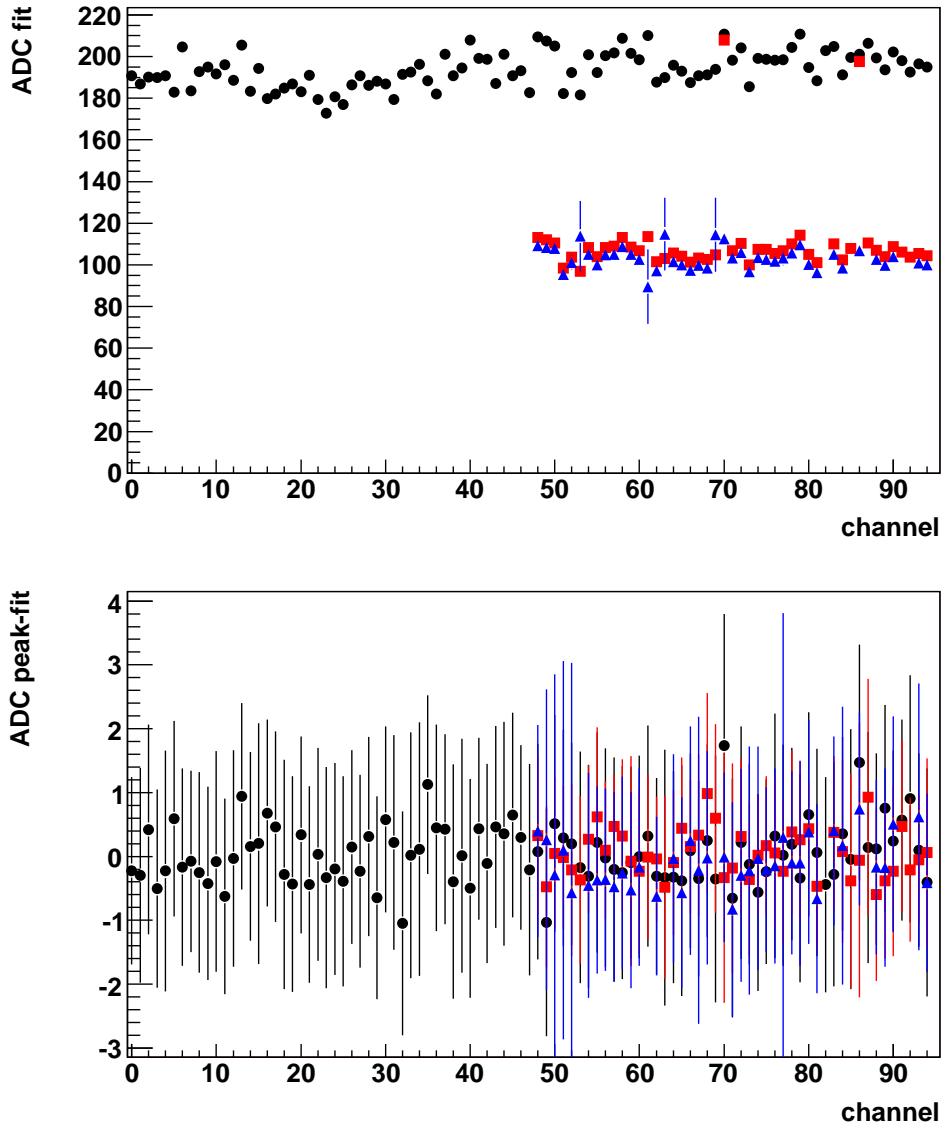
Figure 5: Fit results and comparison of fit with the peak positions of the calibration spectra. The Gd calibration shows two peaks (red and blue), Am only has one peak (black). Error bars are one sigma of gaussian fits.
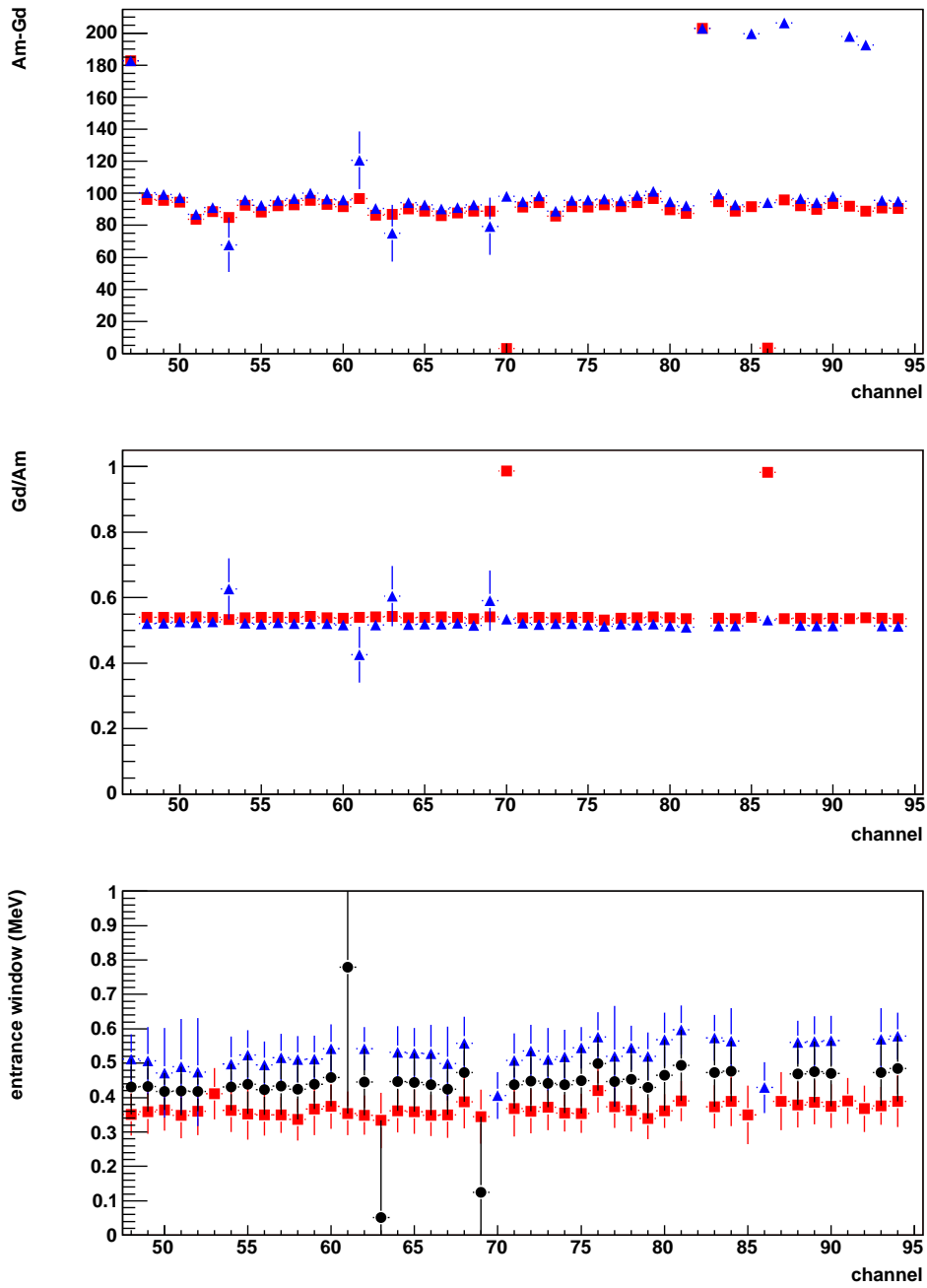
11

Figure 6: Comparison of the Am peaks with both Gd peaks for strips 48 to 95. (Strips 0 to 47 only use Am for calibration.) Red and blue refer to the two Gd peaks; black is an average.

12

$$\begin{aligned}
E_{Am,meas,2,i} &= 5.486 \text{ MeV} - \Delta E_{Am,2,i} &= c_i \cdot ADC_{Am,2,i} \\
E_{Gd,meas,1,i} &= 3.183 \text{ MeV} - \Delta E_{Gd,1,i} &= c_i \cdot ADC_{Gd,1,i} \\
E_{Gd,meas,2,i} &= 3.183 \text{ MeV} - \Delta E_{Gd,2,i} &= c_i \cdot ADC_{Gd,2,i}.
\end{aligned}$$

In principle, there are four equations with five unknowns, $\Delta E_{Am,1}$, $\Delta E_{Am,2}$, $\Delta E_{Gd,1}$, $\Delta E_{Gd,2}$, and c. Assuming, that the differences between ΔE_{Am} and ΔE_{Gd} are small (or known from the stopping power for α-particles), the number of unknowns reduces to three and the linearity of the Silicon strips could be tested. When only one Am peak can be seen in the data, clearly this is not possible. For α-particles, the stopping power drops by almost 30% from 3.2 MeV to 5.5 MeV, so the double peak might just vanish in the energy resolution ($\Delta E_{Am} \approx 0.7 \cdot \Delta E_{Gd}$) [4]. The top part of figure 6 shows the differences between the Am-peak and the two Gd-peaks for strips 48 to 95. Ignoring the few bad fits, the separation between the two differences is nearly constant. Then, the following ratios can be calculated (shown in the middle part of figure 6):

$$\begin{aligned}
r_1 &= \frac{5.486 \text{ MeV} - 0.7 \cdot \Delta E_{1,i}}{3.183 \text{ MeV} - \Delta E_{1,i}} = \frac{ADC_{Am,i}}{ADC_{Gd,1,i}} \\
r_2 &= \frac{5.486 \text{ MeV} - 0.7 \cdot \Delta E_{2,i}}{3.183 \text{ MeV} - \Delta E_{2,i}} = \frac{ADC_{Am,i}}{ADC_{Gd,2,i}}
\end{aligned}$$

The mean ratios are about 0.54 and 0.52, the statistical errors on each point are a little less than half of the difference, indicating that the double Am-peak is actually really lost in the energy resolution. The entrance windows can now be derived from the above equations, see the lower part of figure 6:

$$\begin{aligned}
\Delta E_{1,i} &= \frac{ADC_{Am} - r_1 \cdot ADC_{Gd,1}}{0.7 - r_1} \\
\Delta E_{2,i} &= \frac{ADC_{Am} - r_2 \cdot ADC_{Gd,2}}{0.7 - r_2}
\end{aligned}$$

The mean entrance windows at 3.2 MeV are $\Delta E_1 = 0.365 \pm 0.010$ MeV and $\Delta E_2 = 0.530 \pm 0.012$ MeV for α-particles. Protons lose less than one sixth of this energy, which is less than the energy resolution.

The ADC-to-energy calibration constants are typically in the range of 0.025 to 0.028 MeV per ADC count with uncertainties of 0.0004. They are written to a file data/ADC_Calib.dat.

13

3 Particle Identification

The silicon detectors measure the time-of-flight and the energy of the particles. While this is sufficient for proton identification, the asymmetries have to be determined for elastic proton-proton scattering.

3.1 Elastic Scattering

We are interested in identifying elastic proton proton scattering in the Coulomb nuclear interference region, in the region of the expected peak in analyzing power at $-t \approx 0.003$ (GeV/c^2), as discussed in the introduction. In these collisions, the recoil proton is scattered almost perpendicular to the target, the ejectile continues almost in the beam direction. Due to the very small momentum transfer, the recoil energies are in the range of a few MeV and the reaction can be described by non-relativistic kinematics. For the recoil proton (mass m_P), this means:

$$m_P \approx 2 \cdot T_R \cdot \left(\frac{t_{t.o.f.}}{d(\vartheta_R)} \right)^2 \tag{3}$$

with the time-of-flight $t_{t.o.f.}$, recoil energy T_R, and the distance to the detector $d(\vartheta_R)$. The kinematics of the elastic scattering process of two particles of the same mass correlate the momentum transfer or the recoil energy with the scattering angle ϑ_R:

$$m_P \approx \frac{T_R}{2 \cdot \sin^2 \vartheta_R}. \tag{4}$$

These kinematic correlations are demonstrated in figure 7 using the data for one of the six detector pads for the yellow RHIC beam hitting the jet target. The eight Silicon strips in the down-stream direction detect elastically scattered protons in a certain energy range. Strip #8, in the bottom right figure, is nearly perpendicular to the beam and detects the most peripheral events with the smallest momentum transfer. Decreasing strip numbers are further down-stream, and the recoil energies increases. The spectra in figure 7 have already been filtered for the purpose of an enhanced proton signal. Otherwise, prompt events at small energies and short times-of-flight would dominate the signal even in logarithmic z-scale. The black lines show the fitted range of the proton signal, for details see the next subsection.
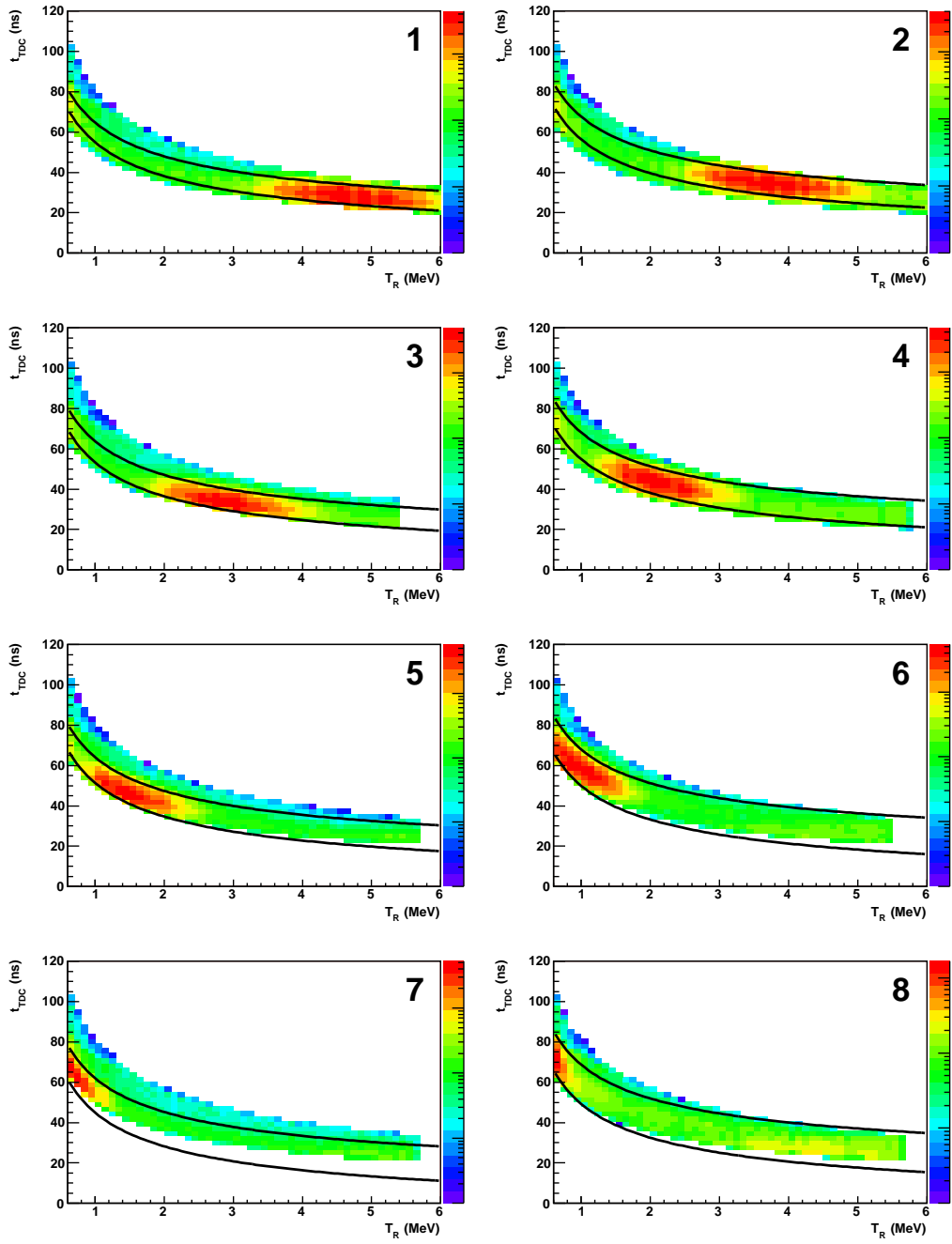
Figure 7: Kinematic correlations for eight strips (1 to 8) of one detector in the time of flight vs. recoil energy distributions.

15

3.2 T_0 Calibrations

After the energy calibration, a time offset has to be determined for each of the silicon strips separately since each has its own electronics chain. The TDC counts are scaled with 1.19 ns for the measured time-of-flight t_{TDC}. From the geometry $d(\vartheta_R)$ and the kinetic energy of the particles T_R, a time-of-flight $t_{t.o.f}$ is calculated. For better visualization, the difference $t_{t.o.f.} - t_{TDC}$ is plotted as a function of the calculated time-of-flight, see center top part of figure 8.

The time offset is determined in several steps. In figure 8, the blue box is set by hand, such that all proton signals are contained within its boundaries for all silicon strips. Then, a projection on the ordinate is fitted with a gaussian, see the top right plot. The mean of the gaussian is displayed in the middle plot with the dashed green line. Second, a projection on the abscissa is used to further constrain the blue box in the x-direction, red lines in the time offset spectrum. The lower right plot shows the projection of the spectrum on the ordinate within the constrained red-blue box, its gaussian fit is represented by the solid green line.

Differences between the two fits are usually not more than a few ns. However, the time offsets on both (yellow and blue signal) sides of the detector have to be determined from the same data set. For the non-signal side, the fit is not always successful in the first approach. Therefore, the procedure is repeated a second time with additional filtering based on the average of the determined time offsets, see figure 9.

Figures 10 to 12 summarize and compare the results of the two repetitions of the fitting procedure for different data sets. The yellow-blue line marks the Silicon strips on the respective signal sides of the detector pads. Figure 10 uses the first data set, in which both RHIC beams have been centered on the jet target (set 0). Differences between the first (green) and the second (red) fit are usually smaller than 1 ns. There are a few strips with large uncertainties, in which the alignment of the detector was such that there was no clear signal on these strips. Figures 11 and 12 show the results for the *120-bunch mode* for only one beam hitting the target. Clearly, one side of the detector gives good results after the first set of fits, while the other side improves considerably in the second approach.

For the final determination of yields, an average time of flight width for proton identification is determined from all strips. The variations in the widths are usually small, although they seem to be consistently increased

16

in the non-signal sides. Using the individual width with an evenly distributed background would lead to strip depencencies and increased background yields, when there is no clear proton signal for the fit.

3.3 Data selection

There are two types of bad waveforms in the discussed data set. For *120-bunch mode* measurements, the waveforms can be late and the tail of the waveform is not recorded in the data acquisition.

The other type of bad waveforms appears in all data sets. Waveforms of this kind are somehow distorted or truncated, the rise and fall-off behaviour is steeper than that of typical waveforms. This might indicate problems with pedestal subtraction, but the details are not understood. These waveforms contribute less than 4% to the total data set and are excluded by a comparison of the integral and the peak ADC information, see figure 15.

3.4 Signal and Background

For elastically scattered protons, the scattering angle is correlated to the recoil energy. Instead of integrating over the entire detectors and all energies, the signal region can be determined as function of energy. Using 0.5 MeV wide energy bins, the peaks of the signals fall within two to three strips, compare figures 7, 13, and 14. Figures 16 and 17 show the elastic proton signals as functions of the Silicon strip number for six different energy bins. The spectra are normalized to the highest yield in a single strip for a given energy bin. The red lines separate the six detectors, the dashed blue lines show the center of each detector separating the yellow (left) and blue (right) signal sides. Energies below 1 MeV are discarded because of an increased background contribution from prompt events. Above 4 MeV, most of the signal is lost from the detector acceptance. The kinematic correlation can be traced along the peak positions moving from the center of the detector to the sides with increasing energy.

Instead of integrating over the whole detector and all energies, the yields are determined only around the peak positions for each selected energy range. This way, the background is reduced by a factor of two to four, depending on the number of strips used for the signal region. (The final asymmetries are calculated with two strips for the signals. For background studies, the number of strip is varied from one to all eight strips.)

3.4.1 Empty target measurements

Empty target measurements have been carried out several times during the 2005 RHIC run by closing the valves of the jet target. This way, the beamgas contribution to the background can be estimated. The yields from these runs are then scaled with the beam intensities integrated over the duration of the measurements. For measurements with one displaced beam, only the intensity of the centered beam should be used for scaling. Usually, differences between relative beam intensities are small, and there is less than a 5% deviation between the results, when the scaling uses both beam intensities. Typically, the beamgas background amounts to about one fourth to one third of the total estimated background.

3.4.2 Abort gaps

For all but the first measurement, one of the two RHIC beams is threaded around the jet target. The effectiveness of the displacement can be tested, by looking at yields for the signal and non-signal sides of the detectors as functions of bunch numbers. Each of the RHIC beams has abort gaps from bunch 112 to 119 which do not contain filled buckets. For the beam that hits the target, the abort gap shows drastically reduced yields, see the upper part of figures 18 and 19. The blue and green curves show the yields for the blue and yellow signal sides (n_s) including all proton identification cuts, the reduced yield is from the respective non-signal side (n_b). Both figures are examples from the *120-bunch* mode, in which the fills did not always have the same number of filled bunches (rising from 60 in the early fills to 111 in the last fills). Summation over all fills then leads to the spiky structure in the bunch distributions.

At IP12 bunch 0 of the blue beam collides with bunch 40 of the yellow beam, indicated by the blue lines in the lower part of the figures. The abort gap of the displaced beam cannot be seen as clearly in the yield distributions. However, if one calculates the ratio of the difference of yields between signal and non-signal sides, divided by the sum, this abort gap becomes visible, too. While the figures only show examples for two measurements for recoil energies 1.5 MeV $< T_R <$ 2.0 MeV, this difference is energy dependent and varies between 1% and 3% in most cases.

Notice also, that the signal side yield in the respective abort gap of the centered beam is still larger (by 20%) than the non-signal side yield. From

this, one can conclude that background from the displaced beam is mainly inelastic and spreads out over the whole detectors. The same is then also true for the inelastic events from the centered beam. Therefore, most of the bunches contain a small amount of contamination from the displaced beam, except those from its abort gap. The step in the difference $(n_s - n_b)/(n_s + n_b)$ is a measure of this effect. Table 3 summarizes this contribution and is later used to estimate the systematic error to describe the results from the *bunch shuffling* method. Comparison with table 2 shows that this type of beam related background amounts to about one third of the total background. Also, there might be overlap with the previously discussed beamgas background.

3.5   Final Data Sets

Tables 4 and 5 present the observed number of events within a 2-strip elastic signal region, for the left (silicon 1,2,3) and right (silicon 4,5,6) counters, for each data set (refer to Table 1 for the data sets). We present the results in 8 columns labeled $N_{left}^{T\uparrow}$ and $N_{right}^{T\uparrow}$ for scattering to beam left, with the target polarized up; $N_{left}^{T\downarrow}$ and $N_{right}^{T\downarrow}$ for scattering to beam left and right with the target polarized down; and four columns for the combinations of left and right scattering with the beam polarized up and down.
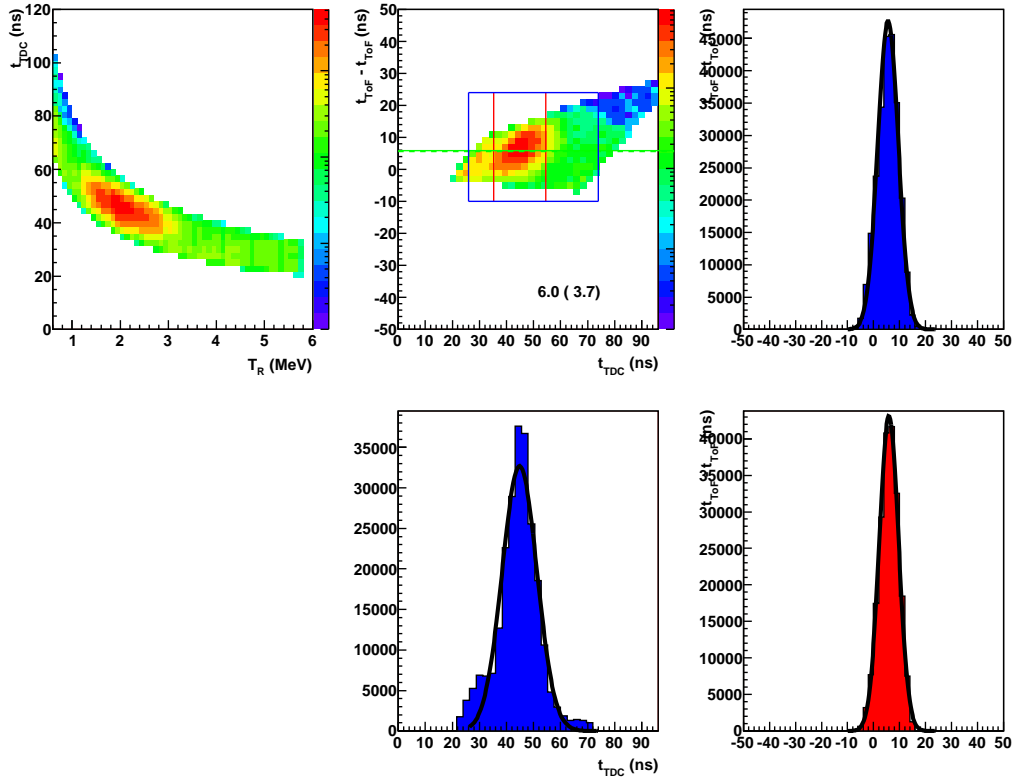
Figure 8: Example of the time-of-flight spectrum and time offset determination for a single silicon strip from the yellow *120-bunch mode* measurement. The top left spectrum (t.o.f. versus recoil energy) is transformed into the top middle spectrum of calculated time-of-flight minus measured TDC counted time. The contents of the blue box are projected onto the ordinate for a first fit of the time offset. A projection onto the abscissa is used to further constrain signal in the blue box within the red boundaries. A second projection of the limited box is fitted for the time offset.
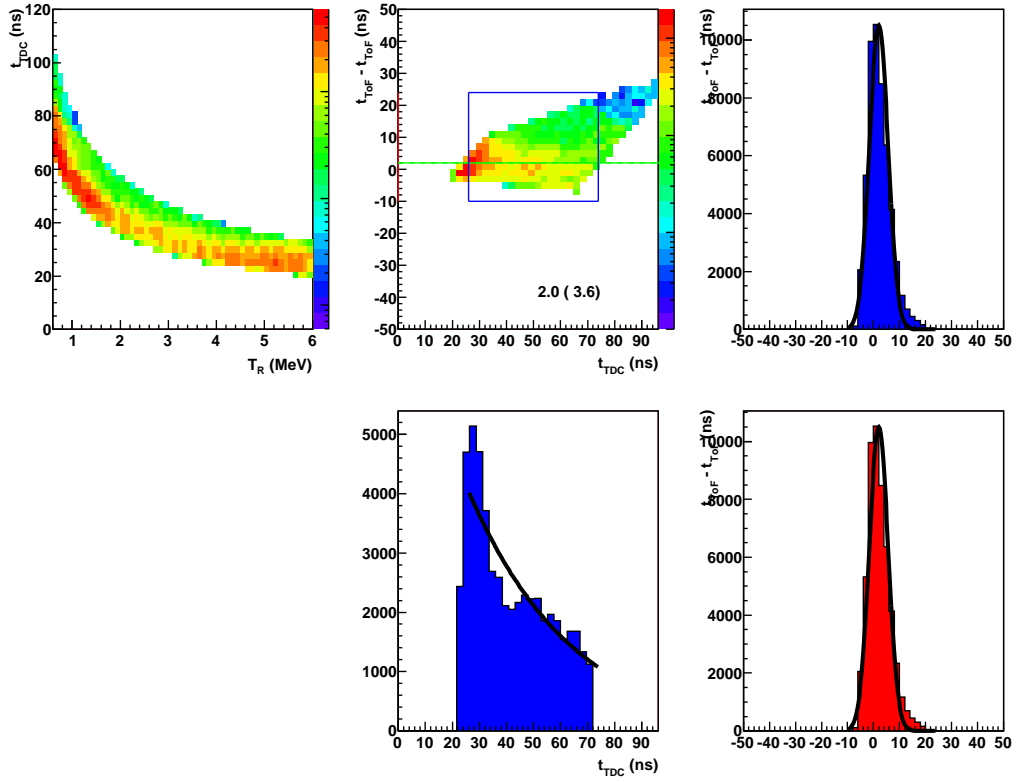
20

Figure 9: Similar to figure 8, proton peaks in the non-signal region of the detector pads have to be determined. The offsets cannot be taken from other measurements, because the clock synchronization changes with the beam that is centered on the jet target.
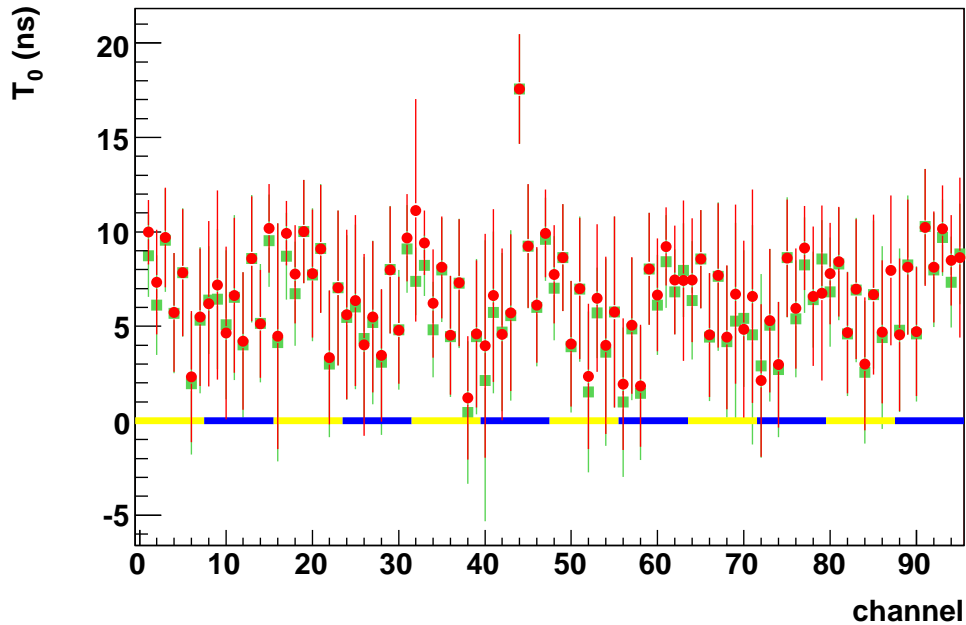
Figure 10: Time-of-flight offset determination for data set 0 (see table 1, both RHIC beams hitting the jet target). Green symbols show the results of the first set of fits, red are the improved fits with additional data filtering.

recoil energy	d-set 2	d-set 3	d-set 4	d-set 5
1.0 MeV $< T_R <$ 1.5 Mev	4.4 %	4.0 %	2.6 %	2.8 %
1.5 MeV $< T_R <$ 2.0 Mev	4.9 %	4.1 %	3.4 %	3.3 %
2.0 MeV $< T_R <$ 2.5 Mev	6.7 %	5.0 %	3.5 %	3.5 %
2.5 MeV $< T_R <$ 3.0 Mev	7.3 %	6.4 %	3.8 %	4.7 %
3.0 MeV $< T_R <$ 3.5 Mev	8.9 %	7.4 %	5.0 %	6.6 %
3.5 MeV $< T_R <$ 4.0 Mev	11.3 %	8.8 %	5.7 %	7.5 %

Table 2: Energy dependent background estimated from the non-signal side of the detectors. Energies below 1 MeV and above 4 MeV are not further considered in the analysis because of increased background and limited acceptance.
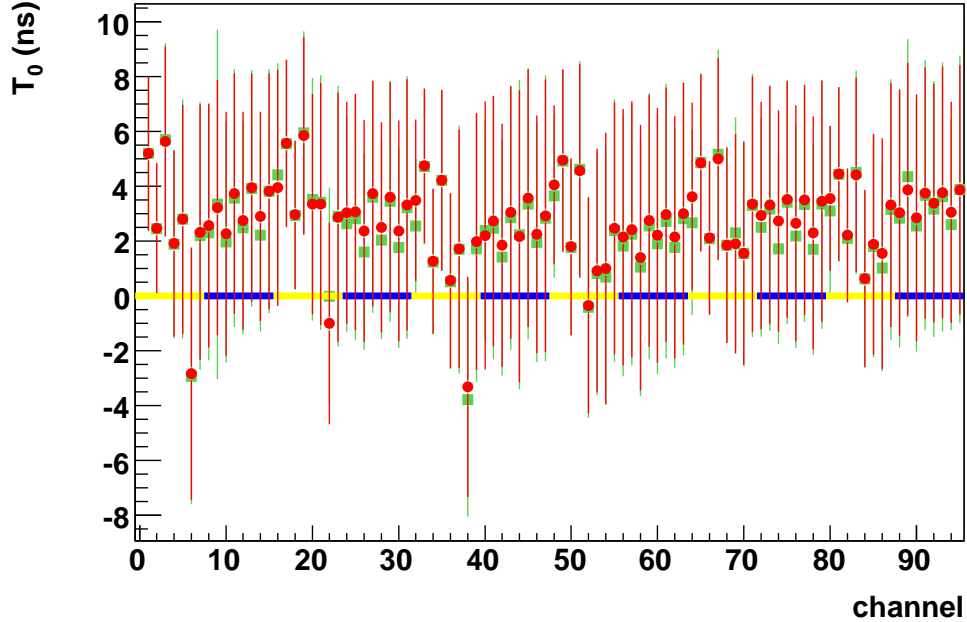
22

Figure 11: Time-of-flight offsets of the yellow beam measurement in *120-bunch mode*. The offsets are comparable to those in figure 10. In both cases the internal clock was synchronized to the yellow RHIC clock.

recoil energy	d-set 2	d-set 3	d-set 4	d-set 5
1.0 MeV $< T_R <$ 1.5 Mev	1.3 %	1.3 %	1.2 %	1.1 %
1.5 MeV $< T_R <$ 2.0 Mev	2.3 %	1.9 %	2.0 %	1.5 %
2.0 MeV $< T_R <$ 2.5 Mev	1.4 %	2.1 %	2.1 %	1.9 %
2.5 MeV $< T_R <$ 3.0 Mev	2.4 %	2.7 %	2.0 %	2.5 %
3.0 MeV $< T_R <$ 3.5 Mev	3.6 %	3.8 %	2.7 %	2.8 %
3.5 MeV $< T_R <$ 4.0 Mev	4.7 %	5.2 %	1.7 %	3.1 %

Table 3: Background contribution from the displaced beam estimated from the bunch distributions, compare figures 18 and 19. The uncertainties are dominated by the number of events in the abort gaps of the displaced beam, giving uncertainties typically less than 0.4%. For data sets 3 and 5, they are 0.2% or smaller.
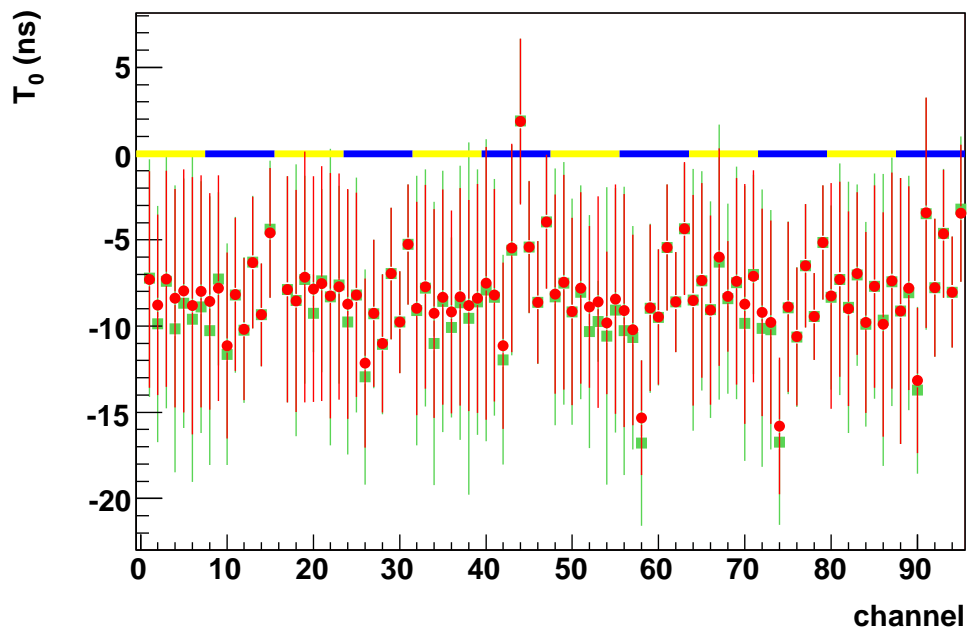
23

Figure 12: Time-of-flight offsets of the blue beam measurement in *120-bunch mode*. The offsets are systematically about 12 ns smaller than those in figure 11 where the internal clock was synchronized to the yellow instead of the blue RHIC clock.
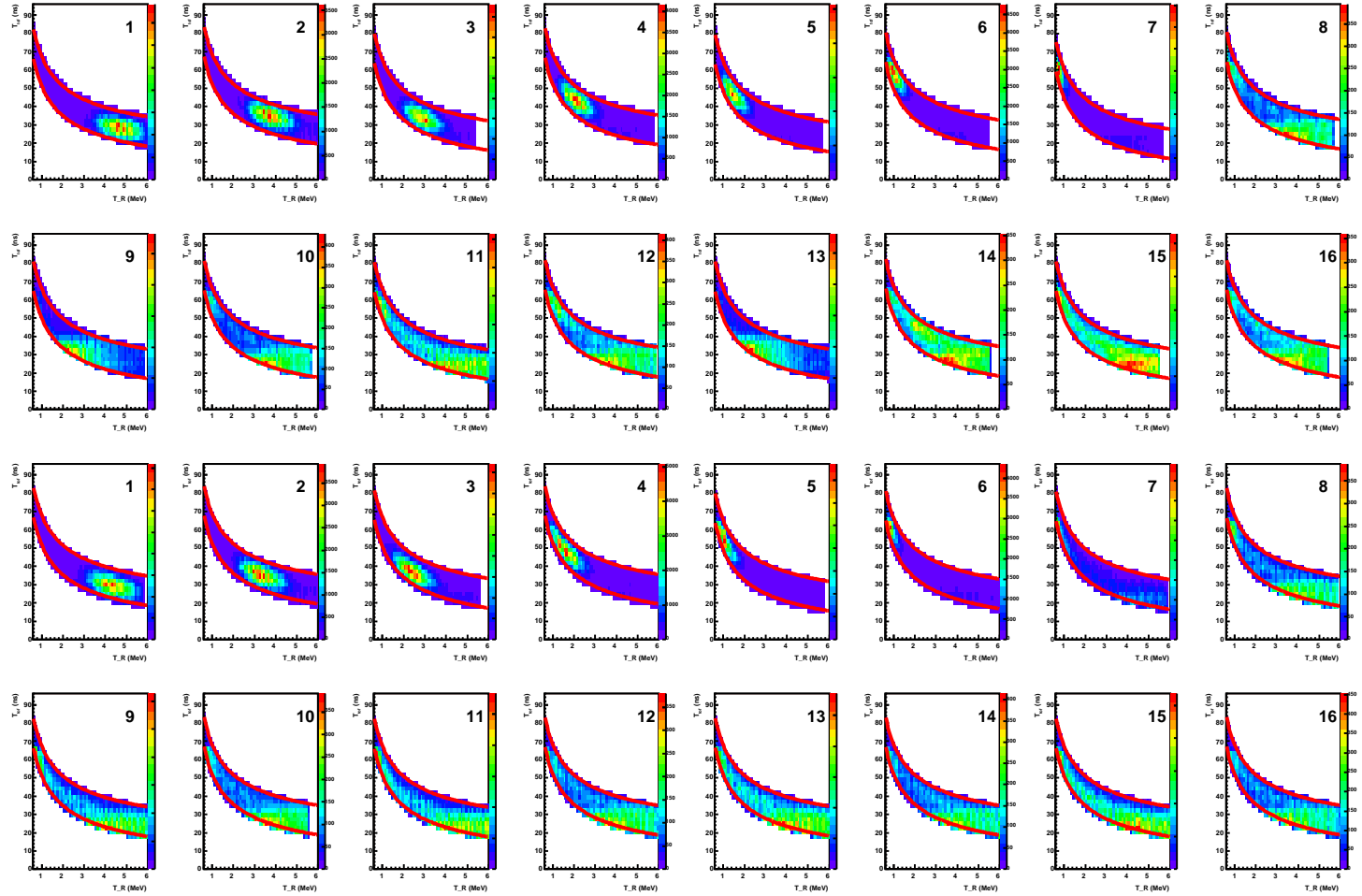
Figure 13: Yields for data sample 3 in strips of detectors 3 and 6. For the yellow beam, the first and third lines are the signal region, lines two and four are the non-signal side.
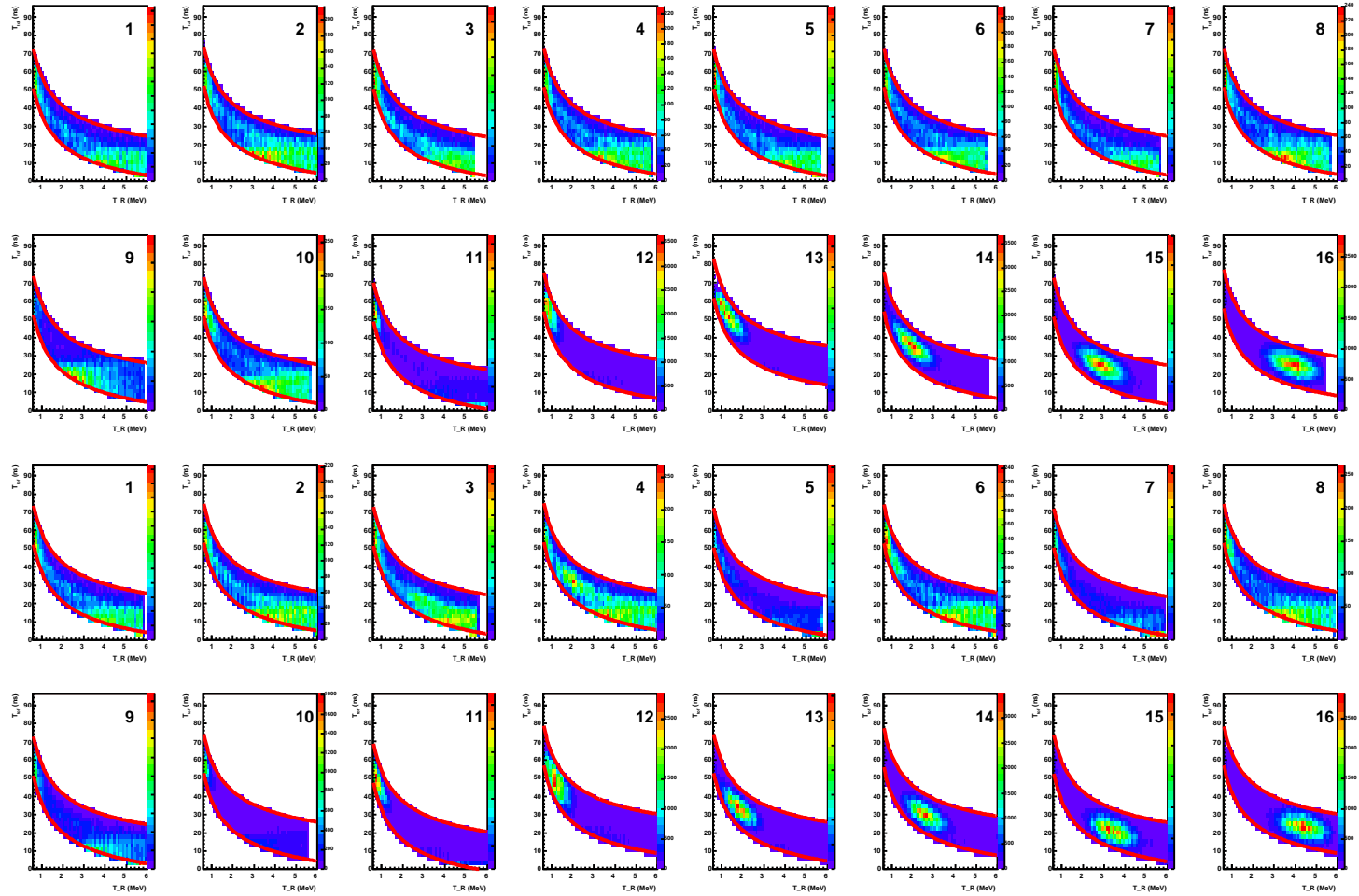
Figure 14: Yields for data sample 5 in strips of detectors 3 and 6. For the blue beam, the second and fourth lines are the signal region, lines one and three are the non-signal side.
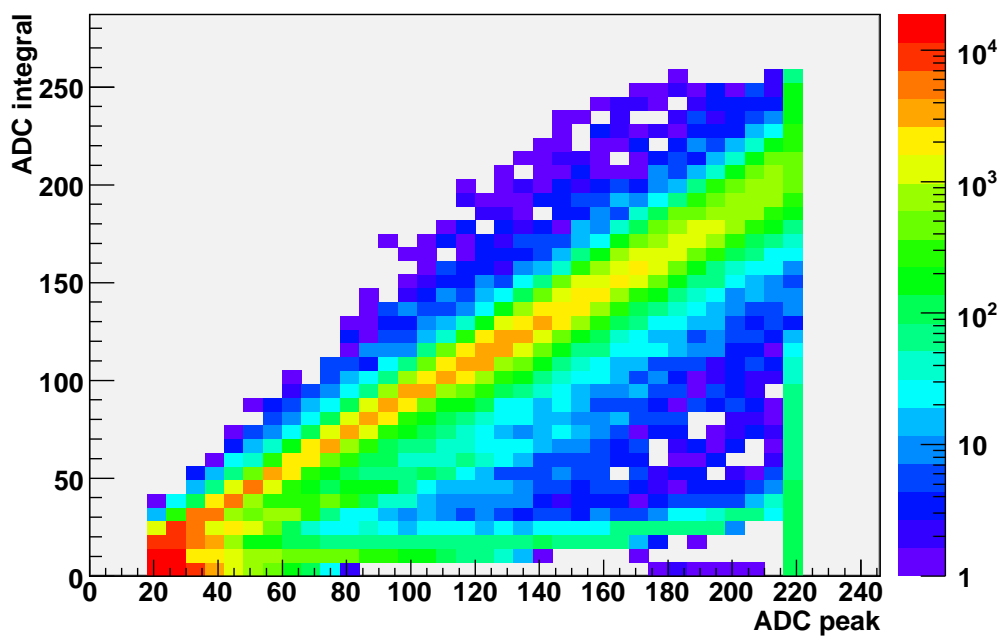
Figure 15: A typical distribution of ADC integral versus ADC peak counts. The lower branch is excluded from the analysis.

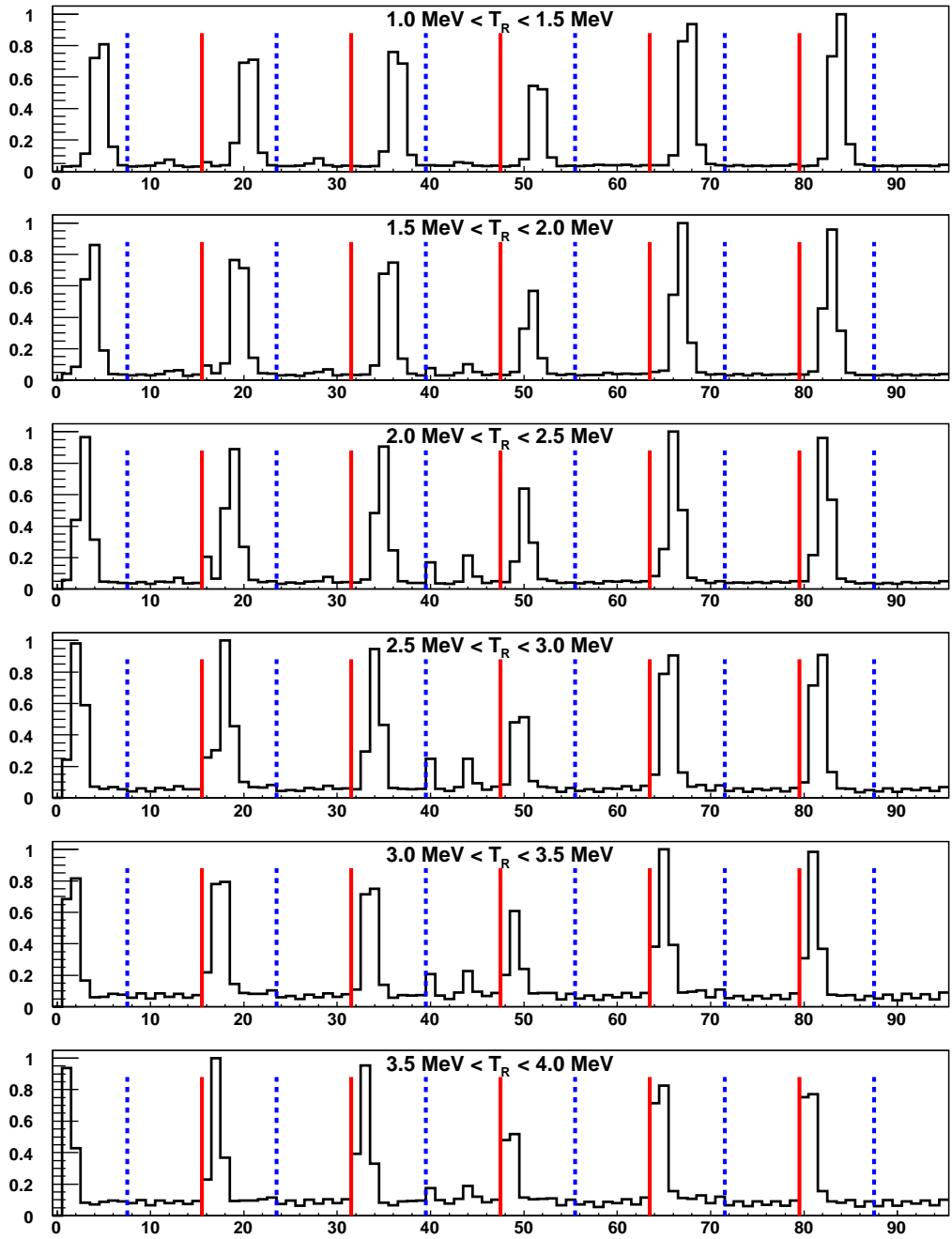Figure 16: Signals peaks in the strip distributions for data set 3. Red lines separate detectors 1 to 6, dashed blue lines show the center of each detector (yellow signals are on the left sides).

28
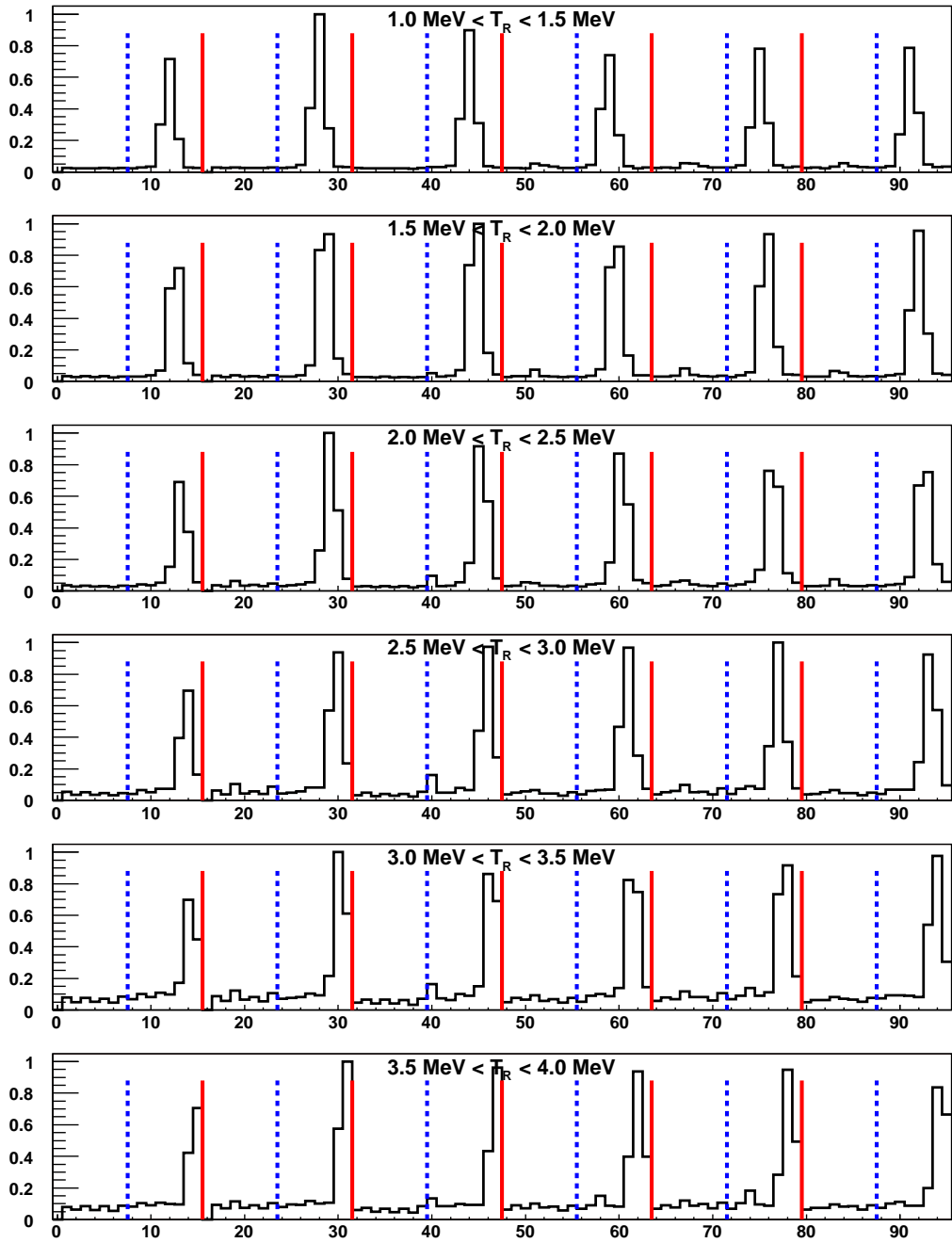
Figure 17: Signals peaks in the strip distributions for data set 5. Red lines separate detectors 1 to 6, dashed blue lines show the center of each detector (blue signals are on the right sides).

29

Figure 18: Yield per bunch integrated over the signal sides (green) and non-signal sides (blue) of all detectors including all proton identification cuts (data set 3, yellow *120-bunch* mode). The bottom plot shows the relative difference between signal and non-signal side yields.
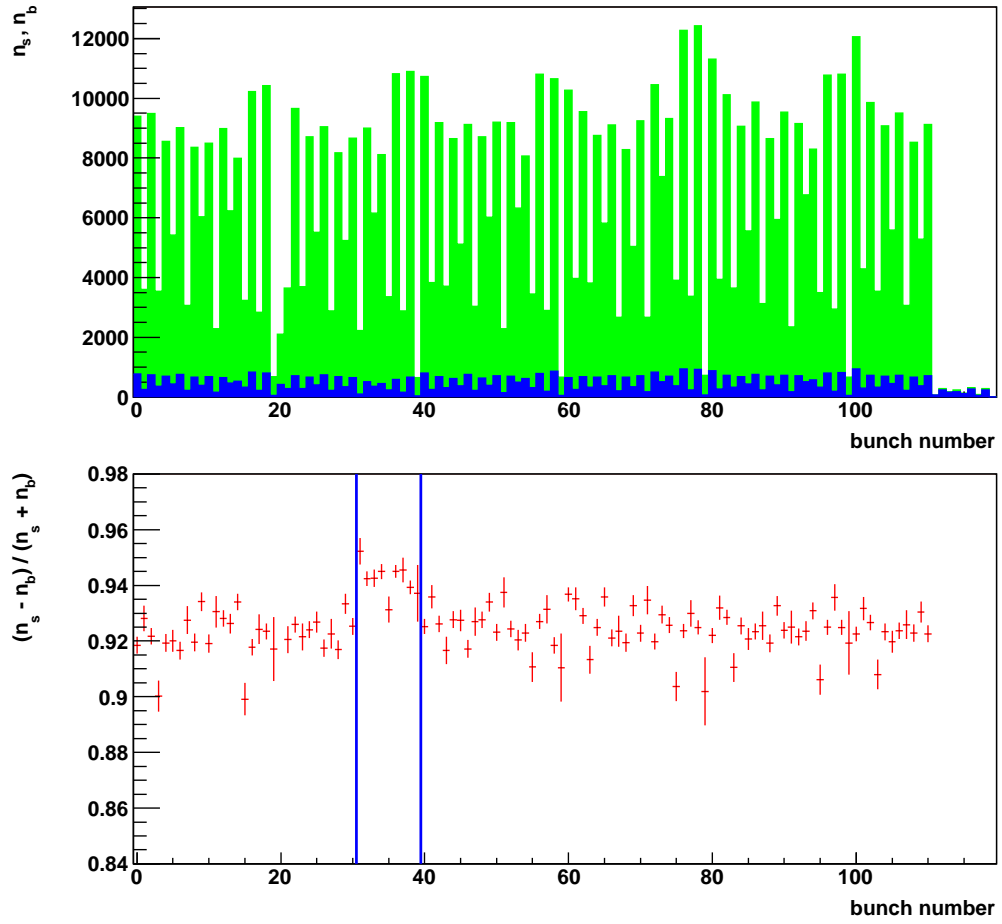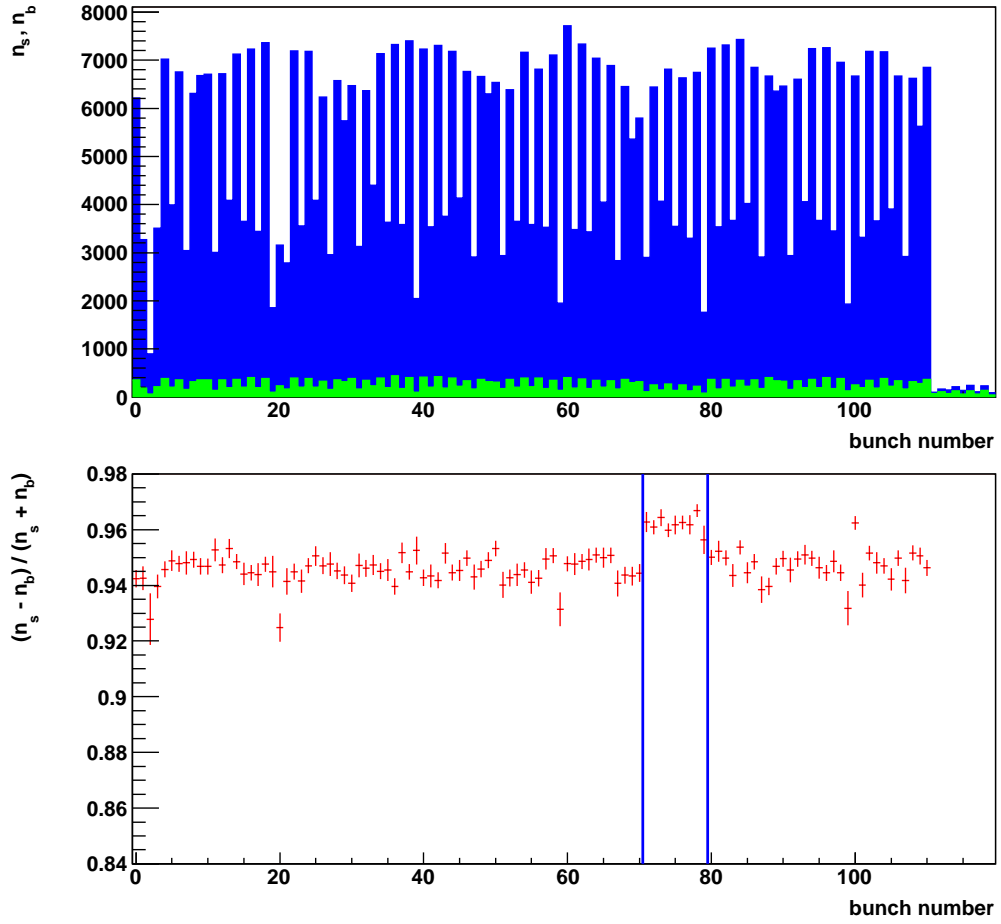
Figure 19: Yield per bunch integrated over the signal sides (blue) and non-signal sides (green) of all detectors including all proton identification cuts (data set 5, blue *120-bunch* mode). The bottom plot shows the relative difference between signal and non-signal side yields.

31

yellow beam	T_R (MeV)	$N_{left}^{T\uparrow}$	$N_{right}^{T\uparrow}$	$N_{left}^{T\downarrow}$	$N_{right}^{T\downarrow}$	$N_{left}^{B\uparrow}$	$N_{right}^{B\uparrow}$	$N_{left}^{B\downarrow}$	$N_{right}^{B\downarrow}$
data set 0	0.80	48255	44850	44538	47309	48007	45985	44786	46174
	1.25	44345	42038	40497	43986	43965	42836	40877	43188
	1.75	35987	32869	32707	34733	35538	33574	33156	34028
	2.25	34062	30920	30885	32561	33641	31806	31306	31675
	2.75	30302	28467	27663	29888	30058	29275	27907	29080
	3.25	31385	24174	29015	25538	31259	25029	29141	24683
	3.75	29542	16547	27440	16883	29623	16762	27359	16668
	5.00	86272	24349	80234	24017	85663	24428	80843	23938
data set 2	0.80	39303	42799	35319	44827	38307	43648	36315	43978
	1.25	40364	39386	36403	42063	39735	40638	37032	40811
	1.75	33869	32290	30386	34223	33175	32991	31080	33522
	2.25	35372	32917	31765	34532	34582	33459	32555	33990
	2.75	34586	28728	31370	30438	33841	29517	32115	29649
	3.25	31906	27074	28631	28315	31211	27619	29326	27770
	3.75	32860	20116	29791	20994	32209	20482	30442	20628
	5.00	85587	28088	78755	28028	84156	28234	80186	27882
data set 3	0.80	128121	108388	125723	124416	130930	116070	122914	116734
	1.25	202219	193750	192697	216643	204581	204137	190335	206256
	1.75	179947	144277	170334	160494	181203	151385	169078	153386
	2.25	157277	136175	148843	152041	157889	143376	148231	144840
	2.75	151112	135896	144384	150528	152537	142514	142959	143910
	3.25	159194	116862	151969	128748	160280	122799	150883	122811
	3.75	135019	125290	130406	138369	136777	131264	128648	132395
	5.00	258003	263685	249994	286485	259996	274889	248001	275281

Table 4: Final numbers of events in the elastic signal region of two strips, for the three data sets with the yellow beam.

blue beam	T_R (MeV)	$N_{left}^{T\uparrow}$	$N_{right}^{T\uparrow}$	$N_{left}^{T\downarrow}$	$N_{right}^{T\downarrow}$	$N_{left}^{B\uparrow}$	$N_{right}^{B\uparrow}$	$N_{left}^{B\downarrow}$	$N_{right}^{B\downarrow}$
data set 0	0.80	49075	49179	50930	45133	48501	47539	51504	46773
	1.25	49029	47877	52307	43199	48756	45847	52580	45229
	1.75	40073	39228	42263	35636	39811	37587	42525	37277
	2.25	33686	38240	35560	34009	33773	36499	35473	35750
	2.75	34633	36462	36521	32949	34395	34745	36759	34666
	3.25	28355	33615	29951	30535	28213	32240	30093	31910
	3.75	20030	33400	20410	30085	19670	31964	20770	31521
	5.00	23121	121832	23030	112545	22856	117569	23295	116808
data set 4	0.80	30482	21791	32740	21078	30538	21579	32684	21290
	1.25	26162	26550	28231	25227	26451	26093	27942	25684
	1.75	23600	24219	26284	22912	24048	23861	25836	23270
	2.25	20936	23823	23254	22377	21460	23224	22730	22976
	2.75	19097	22547	21031	21287	19371	22178	20757	21656
	3.25	18773	21927	20705	20729	19030	21485	20448	21171
	3.75	18146	20043	19747	18863	18429	19546	19464	19360
	5.00	27559	53256	29755	51516	28035	52692	29279	52080
data set 5	0.80	141378	127711	145512	114737	141232	123925	145658	118523
	1.25	143246	143481	148202	127498	142896	138203	148552	132776
	1.75	130871	133364	136042	117778	131142	128674	135771	122468
	2.25	115010	130485	118872	115436	115107	125571	118775	120350
	2.75	106633	122874	109832	109266	105940	118609	110525	113531
	3.25	106047	124684	108633	111680	105365	121169	109315	115195
	3.75	101961	114084	104840	102248	101634	110202	105167	106130
	5.00	157828	310933	160029	283065	156972	302513	160885	291485

Table 5: Final numbers of events in the elastic signal region of two strips, for the three data sets with the blue beam.

4 Asymmetries

4.1 Square-root Asymmetries

All final asymmetries have been calculated with the *square-root* formula [5]. This analysis method uses a geometrical mean to obtain an estimate of the number of counts, comparing data from polarization up and down directions (target or beam) and left and right scattering. This approach can also be used to determine the acceptance or luminosity asymmetries. Below, ϵ refers to the physics asymmetry, which in the case of the polarized proton beam scattering elastically from the polarized proton target can be calculated for a polarized beam, summing over the spin states of the target to obtain an unpolarized target, and can be calculated for a polarized target, summing over the spin states of the polarized beam to obtain an unpolarized beam. [3] $\epsilon_{acceptance}$ is the acceptance asymmetry, and $\epsilon_{rel-lumi}$ is the asymmetry of the luminosities for up and down polarized target or beam:

$$\epsilon = \frac{\sqrt{N_{left}^{\uparrow} \cdot N_{right}^{\downarrow}} - \sqrt{N_{left}^{\downarrow} \cdot N_{right}^{\uparrow}}}{\sqrt{N_{left}^{\uparrow} \cdot N_{right}^{\downarrow}} + \sqrt{N_{left}^{\downarrow} \cdot N_{right}^{\uparrow}}} \tag{5}$$

$$\epsilon_{acceptance} = \frac{\sqrt{N_{left}^{\uparrow} \cdot N_{left}^{\downarrow}} - \sqrt{N_{right}^{\uparrow} \cdot N_{right}^{\downarrow}}}{\sqrt{N_{left}^{\uparrow} \cdot N_{left}^{\downarrow}} + \sqrt{N_{right}^{\uparrow} \cdot N_{right}^{\downarrow}}} \tag{6}$$

$$\epsilon_{rel.lumi} = \frac{\sqrt{N_{left}^{\uparrow} \cdot N_{right}^{\uparrow}} - \sqrt{N_{left}^{\downarrow} \cdot N_{right}^{\downarrow}}}{\sqrt{N_{left}^{\uparrow} \cdot N_{right}^{\uparrow}} + \sqrt{N_{left}^{\downarrow} \cdot N_{right}^{\downarrow}}} \tag{7}$$

Figures 20 and 21 shows results for data sets 3 and 5 of the square root asymmetries at recoil energies $1.5 \, \text{MeV} < T_R < 2.0 \, \text{MeV}$. The vertical dashed lines separate the three detector pairs. Both the physical and the luminosity asymmetries are emerging in the strips of the signal region. Although the stastical accuracy is lacking, we see no indication of an asymmetry in the background strips.

---

[3]Residual polarization, for example for residual target polarization in the beam asymmetry ϵ_{beam}, contributes at third order, with a correction factor of $\epsilon_{beam} \times (1 + (A_N P_T \epsilon_{rel.lumi}^{Target})^2)$. For the observed values of $\epsilon_{rel.lumi}^{Target}$=0.02, this correction is about $10^{-6} \times \epsilon_{beam}$.
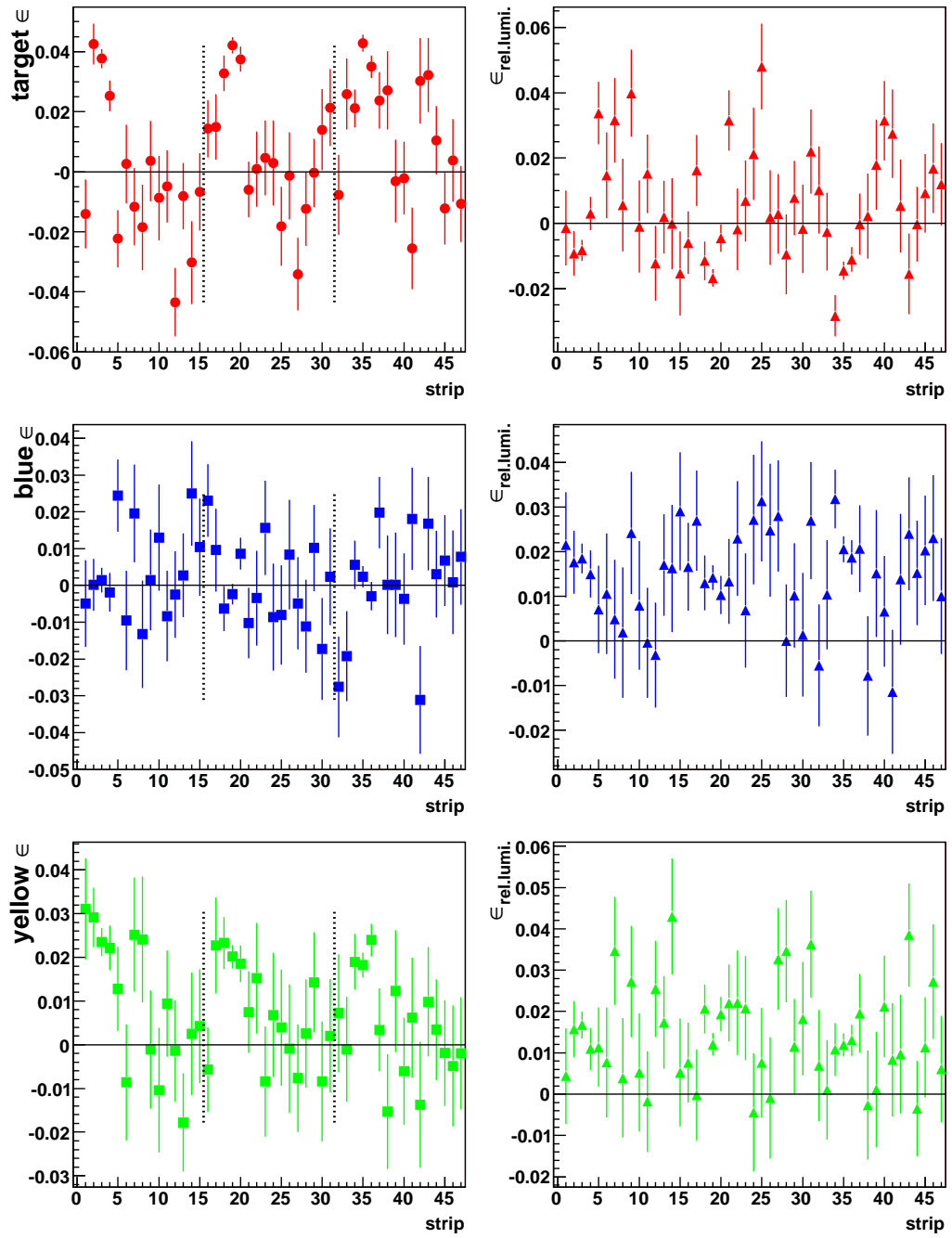
Figure 20: Square root asymmetries for data set 3 at recoil energies 1.5 MeV $< T_R <$ 2.0 MeV.

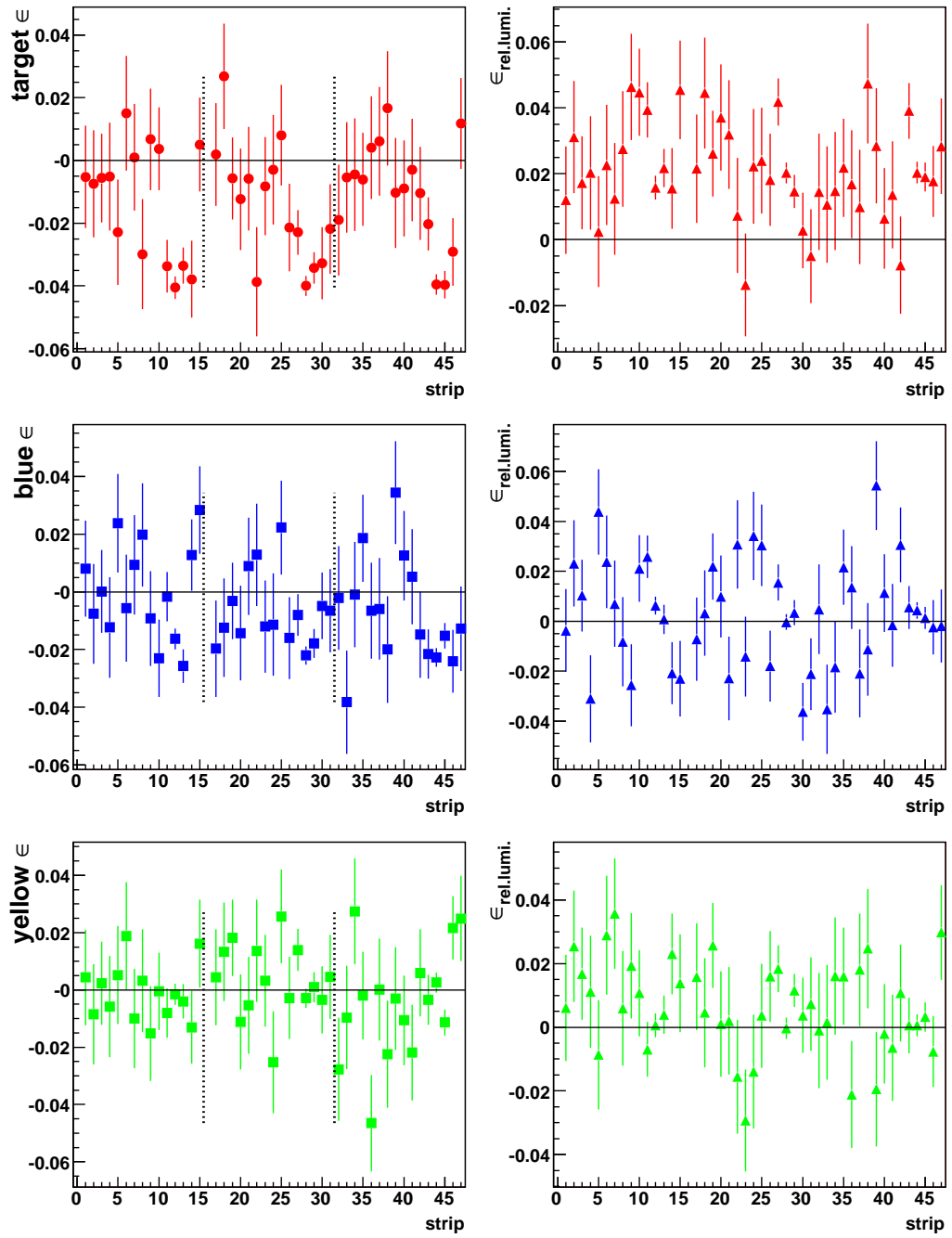Figure 21: Square root asymmetries for data set 5 at recoil energies 1.5 MeV $< T_R < 2.0$ MeV.

Figures 22 and 23 use the combined yields of all left and right side detectors, that have been kept separated in figures 20 and 21. The vertical dashed lines here divide the signal side on the detectors from the non-signal sides. Again, no indication of any background asymmetry can be seen within the statistical errors. The luminosity asymmetries are also shown; they are the same for the three elastic signal regions for the three detector pairs, and show some variation for the background regions.

After extensive cross checks with simple and square-root asymmetries, we go on to calculate the asymmetries as functions of recoil energy T_R only within the determined signal strips. These asymmetry calculations use the measured number of elastic events given in tables 4 and 5. The results are presented for each data set in tables 6 and 7. Note that the uncertainties for the asymmetries are $\Delta\epsilon = 1/\sqrt{N_{total}}$, where N_{total} is the total number of events, and the uncertainty is the same for the beam and target asymmetries. The table also presents the asymmetry ratio $r = \epsilon_{beam}/\epsilon_{target}$, and its uncertainty. This uncertainty is $\delta r/r = (1/A_N) \times \sqrt{1/P_{beam}^2 + 1/P_{target}^2} \times \sqrt{1/N_total}$. with $P_{beam} = r \times P_{target}$ and P_{target} independently measured. A_N is obtained from the target asymmetry and target polarization, $A_N = \epsilon_{target}/P_{target}$.

Figures 24 to 27 present the asymmetry results and asymmetry ratios for data sets 2 through 5. The measured asymmetries are compared to an existing formal description of the analyzing power A_N in terms of helicity amplitudes ϕ_1 to ϕ_5 [1], which is scaled with the jet target polarization (solid red line) and the determined beam polarization (dashed green or blue line). These curves are not fitted to the data and are only meant to guide the eye.

Energies below $T_R = 1$ MeV and above $T_R = 4$ MeV are not considered further for the beam polarization determination because of asymmetric acceptance and increased background (note the drop-off in all asymmetries above 4 MeV).

The beam polarization P_{beam} is derived from the target (ϵ_{target}) and the beam (ϵ_{beam}) related asymmetries and the independently measured target polarization P_{target}:

$$\frac{P_{beam}}{P_{target}} = \frac{\epsilon_{beam}}{\epsilon_{target}}. \tag{8}$$

The errors for the asymmetry ratios, presented above with the table, are calculated from the independent measurements of the numbers of elastic events given in tables 4 and 5, and are identical to the result of treating the measurements of ϵ_{beam} and ϵ_{target} as independent measurements. We
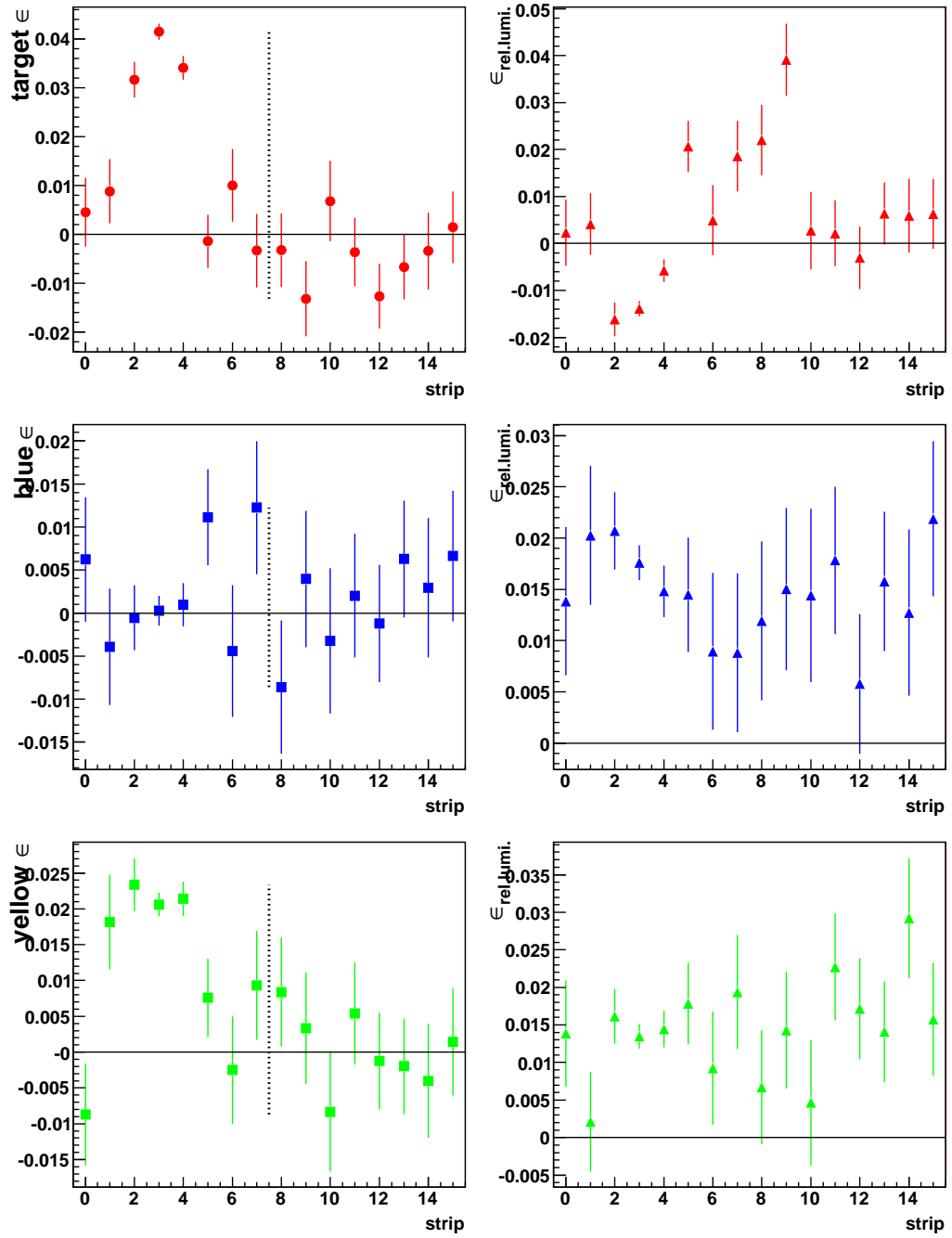
Figure 22: Square root asymmetries for data set 3 at recoil energies 1.5 MeV $< T_R <$ 2.0 MeV.

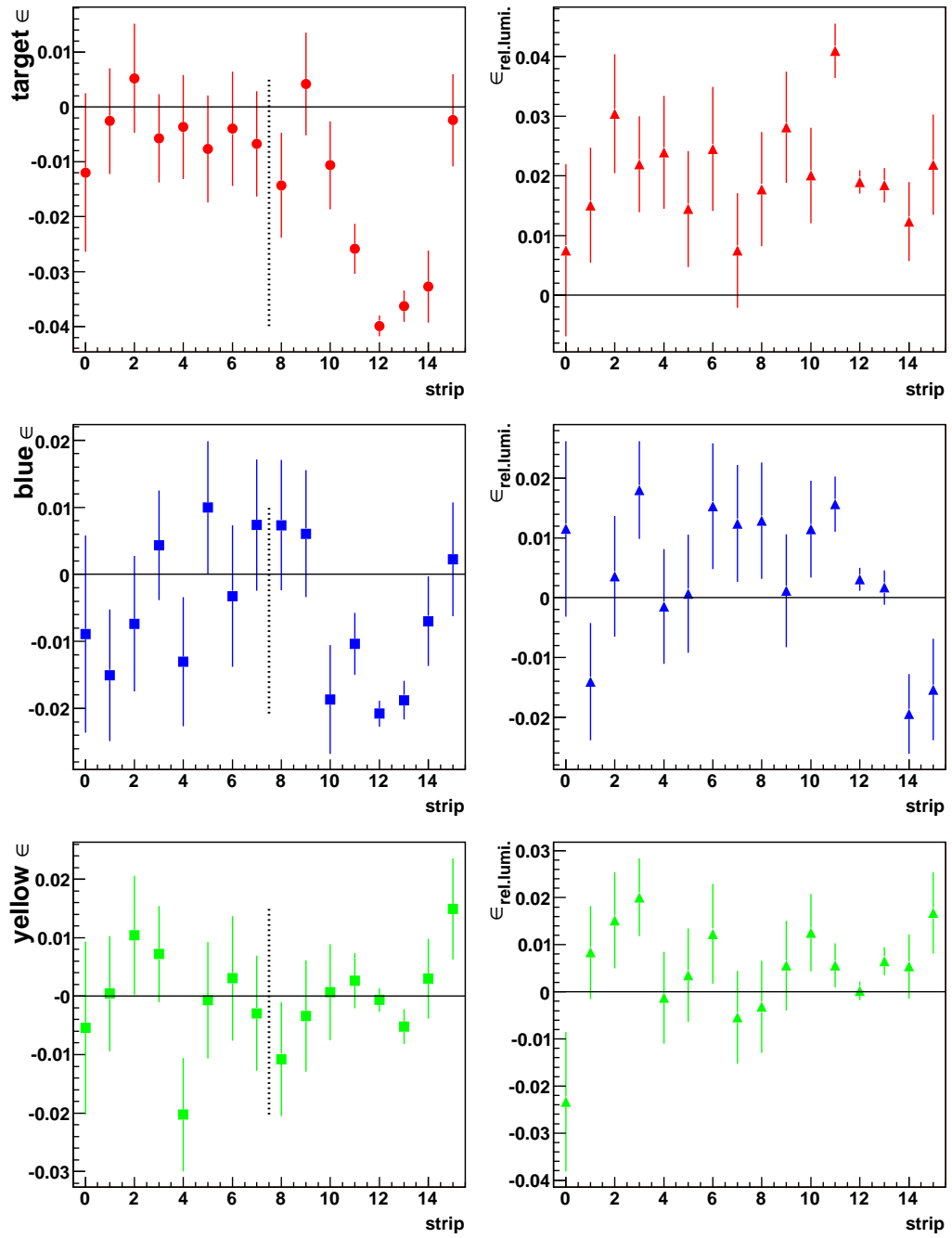Figure 23: Square root asymmetries for data set 5 at recoil energies 1.5 MeV $< T_R < 2.0$ MeV.

| yellow beam | T_R | ϵ_{target} | ϵ_{beam} | $\Delta\epsilon$ | $r = \frac{\epsilon_{beam}}{\epsilon_{target}}$ | Δr |
	(MeV)	(%)	(%)	(%)	(%)	(%)
	1.25	3.40	2.02	0.24	59.6	8.3
	1.75	3.77	2.07	0.27	55.0	8.2
data	2.25	3.74	1.70	0.28	45.3	8.2
set 0	2.75	3.49	1.69	0.29	48.3	9.3
	3.25	3.33	1.41	0.30	42.2	9.9
	3.75	2.35	1.85	0.34	78.7	18.7
	1.0-4.0				51.8	3.8
	1.25	4.22	1.87	0.25	44.2	6.5
	1.75	4.16	2.03	0.28	48.7	7.4
data	2.25	3.88	1.90	0.27	49.0	7.8
set 2	2.75	3.88	1.42	0.28	36.6	7.8
	3.25	3.83	1.69	0.29	44.3	8.4
	3.75	3.52	1.59	0.32	45.1	9.9
	1.0-4.0				44.7	3.2
	1.25	4.00	2.06	0.11	51.6	3.1
	1.75	4.03	2.06	0.12	51.1	3.4
data	2.25	4.13	1.83	0.13	44.3	3.4
set 3	2.75	3.69	1.86	0.13	50.5	4.0
	3.25	3.58	1.51	0.13	42.2	4.1
	3.75	3.35	1.75	0.14	52.1	4.6
	1.0-4.0				48.7	1.5

Table 6: Final asymmetries in the elastic signal region of two strips, for the three data sets with the yellow beam.

blue beam	T_R (MeV)	ϵ_{target} (%)	ϵ_{beam} (%)	$\Delta\epsilon$ (%)	$r = \frac{\epsilon_{beam}}{\epsilon_{target}}$ (%)	Δr (%)
	1.25	4.19	2.23	0.23	53.2	6.2
	1.75	3.73	1.86	0.25	49.8	7.6
data	2.25	4.28	1.75	0.27	40.8	6.7
set 0	2.75	3.86	1.72	0.27	44.5	7.6
	3.25	3.77	1.87	0.29	49.6	8.5
	3.75	3.08	1.71	0.32	55.5	11.8
	1.0-4.0				48.2	3.1
	1.25	3.18	1.77	0.31	55.5	11.0
	1.75	4.08	2.42	0.32	59.3	9.2
data	2.25	4.19	1.71	0.33	40.7	8.6
set 4	2.75	3.85	2.32	0.35	60.4	10.5
	3.25	3.85	2.16	0.35	56.2	10.4
	3.75	3.63	1.60	0.36	44.2	10.9
	1.0-4.0				52.2	4.1
	1.25	3.80	1.97	0.13	51.9	4.0
	1.75	4.07	2.10	0.14	51.6	3.8
data	2.25	3.89	1.85	0.14	47.5	4.1
set 5	2.75	3.67	2.15	0.15	58.6	4.7
	3.25	3.35	2.18	0.15	65.1	5.3
	3.75	3.43	1.80	0.15	52.3	5.1
	1.0-4.0				53.5	1.8

Table 7: Final asymmetries in the elastic signal region of two strips, for the three data sets with the blue beam.
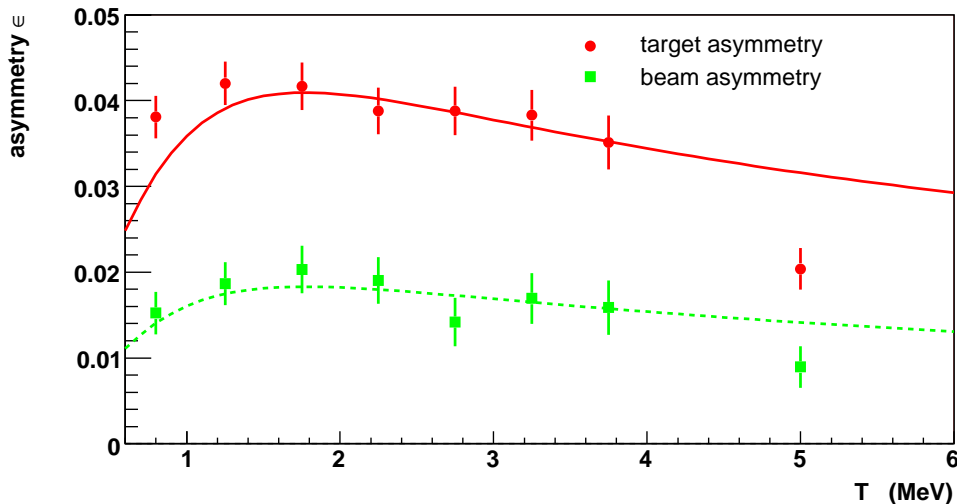
Figure 24: Square root asymmetries for data set 2 (yellow beam, *60-bunch* mode) as functions of recoil energy T_R.

determine a T_R-dependent asymmetry ratio mainly to reduce the contained background in the yields, before calculating the weighted mean. Cross checks with integrated yields show that the functional form of A_N is negligible for the determination of the beam polarization.

4.2   Background Contributions in Asymmetry Ratios

As shown in the previous chapter (table 2), the background below the signal region can be estimated from the non-signal sides of the detectors. This background can be as large as 10% of the signal height and in the following leads to reduced asymmetries by the same fraction. If the background is polarization dependent, this must also be considered in the determination of the analyzing power.

For the 2005 data, the primary objective is the determination of the beam polarization and not the analyzing power of elastic proton-proton scattering itself. Therefore, combination of equation 8 with the respective asymmetry formulas removes polarization independent background from the beam polarization result. For simple asymmetries, the denominator of both asymmetries (i.e. the sum over both polarization states) is the same, while the numerator (the difference of both polarization states) removes all polarization
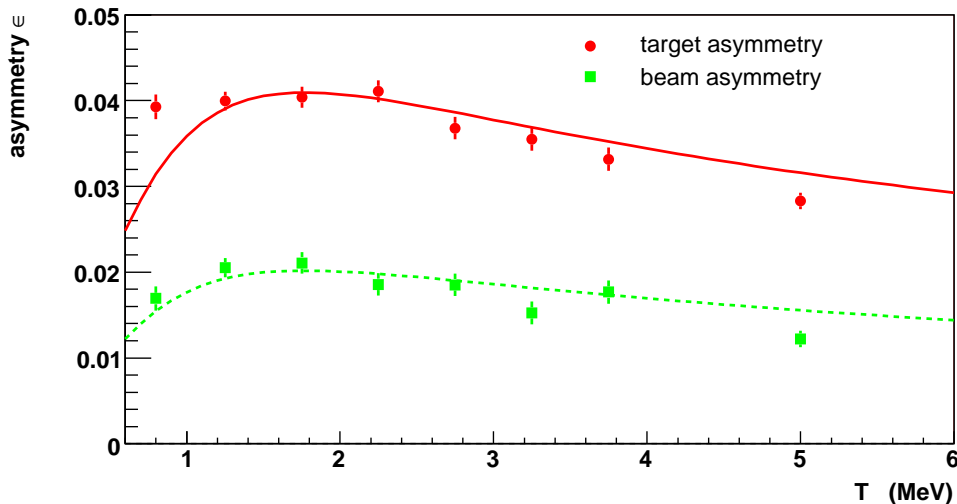
Figure 25: Square root asymmetries for data set 3 (yellow beam, *120-bunch mode*) as functions of recoil energy T_R.

independent contributions completely. For the square root asymmetries, the correction is below 10^{-4} on the ratio P_B/P_T for a 5% unpolarized background contribution.[4]

Studies have been carried out to determine a limit on the asymmetry ratio from possibly polarized background by varying the measured background contributions near the elastic $p + p$ signal. The strip distributions show a uniformly spread yield over the non-signal strips. By increasing the number of strips for the elastic peak, the background contributions can be increased in a controlled way. The minimum number of strips for the signal is, of course, one. This can be increased to up to eight strips. Figures 28 and 29 show the corresponding results to the previous set of figures. The right parts of the figures summarize the asymmetry ratios for different numbers of strips for the signal region, going from one to eight. The original asymmetries were calculated with two strips, again corresponding to the solid symbols on the left sides of the figures. The open symbols on the left refer to four and eight strips, thereby doubling and quadrupling the background contributions.

---

[4]The correction is $(\beta/(1 + \beta^2)) \times A_N^2 \times (P_{target}^2 - P_{beam}^2)$, where β is the fraction of unpolarized background/elastic signal. We also artificially added polarization independent background yields of up to 50% of the signal yield. While the asymmetries drop accordingly, the asymmetry ratio is affected by less than 1%.
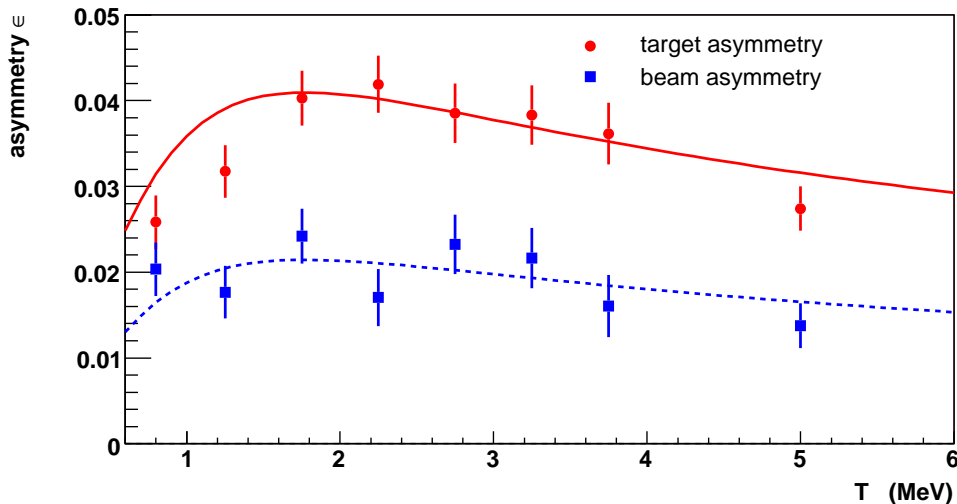
Figure 26: Square root asymmetries for data set 4 (blue beam, *60-bunch mode*) as functions of recoil energy T_R.

While the variations are smaller than the statistical errors, these differences do not necessarily point to a polarization dependence of inelastic events but might well be just statistical fluctuations.[5] Also, no clear asymmetry has been seen in figures 20 through 23.

The conclusion from the variations of signal strips is that the background yields below the elastic peak contribute at most 1.1% to the asymmetry ratio, where we use the largest change observed. The systematic error for the beam polarization scales with the target polarization, accordingly.

4.3   Bunch Shuffling

Certain beam related systematic errors can be explored with the *bunch shuffling* technique. In this method, the polarization direction of each RHIC bunch is randomly assigned and the resulting asymmetries are calculated.[6]

---

[5]The deteriorating statistical accuracy is less obvious, because the single strip results contain only about half of the elastic statistics of two strips and there can also be elastic events in a third strip. Again, the blue asymmetry ratio seems to drop slightly, and the yellow asymmetry rises.

[6]While a randomized polarization pattern and randomization of single events both lead to an unpolarized beam, the first approach still assumes polarization of single bunches and

This process is repeated several thousand times. Systematic errors are diluted by the statistical accuracy of the data sample, which is usually the dominant part of the uncertainties.

The bunch shuffling results are shown in figures 30 and 31 for the two data sets with the highest statistics. Beam asymmetries were calculated as weighted means for separate recoil energies, the target asymmetries were not considered. Asymmetries from integrated yields over all energies have been cross checked and show similar results. Each figure contains 5000 iterations of the randomization process and the asymmetries have been scaled with reciprocal statistical errors. The average asymmetry should be zero by construction. The distributions for the randomized patterns are gaussian with a width of one if the associated errors are purely stochastic. Gaussian fits to the distributions are also included in the figures and they describe the shape well for all asymmetries.

Emphasis has to be put to the yellow beam (green curve) in figure 30 and the blue beam in figure 31, compare table 8. In both cases, the width is slightly enhanced. The number of bunches n can have an effect on the width of the distributions, leading to larger deviations for fewer bunches that are part of the randomization:

$$\sigma_{shuffle} = \frac{1}{\sqrt{n-1}}. \tag{9}$$

The average number of bunches for the relevant data sets is 80 to 100, leading to $\sigma_{shuffle} \approx 0.12$, which still does not cover the observed widths. Obviously, for these two data sets the statistical accuracy is in the range of an emerging systematic uncertainty. The other data sets have significantly less statistics, which does not mean that they don't suffer from the same systematic errors. It is further noticeable, that the displaced beam asymmetries do not show the same discrepancies.

Table 8 indicates that there is some beam related systematic uncertainty. Differences between yields for different bunch numbers have been seen and have been associated to the displaced beam, the beam threaded around the target, compare abort gap studies in the previous chapter. A rough estimate of the systematic error arising from these differences has been added to the statistical errors and the total error has then been used in the bunch shuffling. As a result, the widths of the problematic beams fall off to 1.09 and 1.13 and are consistent with one. All other widths are minimally, if at all, affected.

---

is sensitive to differences between separate bunches.

data set	$\bar{\epsilon}_{blue}$	$\sigma(\bar{\epsilon}_{blue})$	$\bar{\epsilon}_{yellow}$	$\sigma(\bar{\epsilon}_{yellow})$
0	0.018	1.06	0.014	1.09
2	-0.043	1.01	-0.021	1.11
3	-0.005	1.11	0.005	1.32
4	-0.007	1.07	-0.007	1.02
5	0.014	1.27	-0.013	1.03

Table 8: Results from the bunch shuffling method. For data sets 3 and 5, the centered beam asymmetry distributions show an increased width ($\bar{\epsilon}_{yellow}$ for data set 3 and $\bar{\epsilon}_{yellow}$ for data set 5).

data set	beam	$r = \epsilon_{beam}/\epsilon_{target}$	σ_r	P_{beam}	$\sigma_{P_{beam}}(stat)$
0	yellow	0.5183	0.0381	47.89%	3.52%
0	blue	0.4821	0.0309	44.55%	2.86%
2	yellow	0.4466	0.0317	41.27%	2.93%
3	yellow	0.4872	0.0151	45.02%	1.40%
4	blue	0.5220	0.0406	48.23%	3.75%
5	blue	0.5353	0.0179	49.46%	1.65%

Table 9: Results of the asymmetry ratios, beam polarizations, and statistical errors.

4.4   Beam Polarizations

The final asymmetry ratios and beam polarizations with their statistical errors are summarized in table 9. The beam polarizations are obtained from the asymmetry ratios presented in tables 6 and 7, using the independently measured jet polarization discussed in Section 2.1. The jet polarization was $P_{target} = (92.4 \pm 1.8)\%$, with the uncertainty from estimating the unpolarized molecular contribution to the polarized atomic hydrogen jet target. The uncertainties in the table are statistical. The global systematic uncertainty is obtained from the quadratic sum of the molecular fraction uncertainty and the background uncertainty for the asymmetry ratio r: $\Delta P_{beam}/P_{beam}(syst) = \sqrt{(0.018/P_{target})^2 + (0.011/r)^2}$. With $r \approx 0.5$, this is $\Delta P_{beam}/P_{beam}(syst) = \pm\sqrt{0.0195^2 + 0.022^2} = \pm 0.029$.

Figure 32 shows a comparison of the final polarization values determined

with the jet polarimeter with online numbers taken with the Carbon polarimeters (blue in the top and yellow in the bottom part of the figure). The abscissa is in units of days, starting shortly before April 22 and running until June 24. The online numbers are displayed by the red circles. Underlying the circles are colored (blue and yellow) boxes which indicate a $\pm$ one sigma band of the jet polarization in the respective data sub-sample. The vertical dashed line show a change of the jet polarimeter target setup, either a change in the *60/120-bunch* mode, movement/displacement of RHIC beams, or change of RHIC energies. For reference, each of the sub-figures contains a colored band starting with green on the left side. Green regions refer to the *both-beam* mode in the beginning of the run. Yellow and blue regions are, of course, measurements with the blue (yellow, resp.) beam displaced. Dashed bands indicate the *60-bunch* mode, filled bands are measurements in the *120-bunch* mode. Also, there is a short magenta region of 205 GeV/c commissioning, where the data are not presented. Near the right edge, a few measurements in a single fill have been excluded from the jet analysis because both beams were slightly displaced.
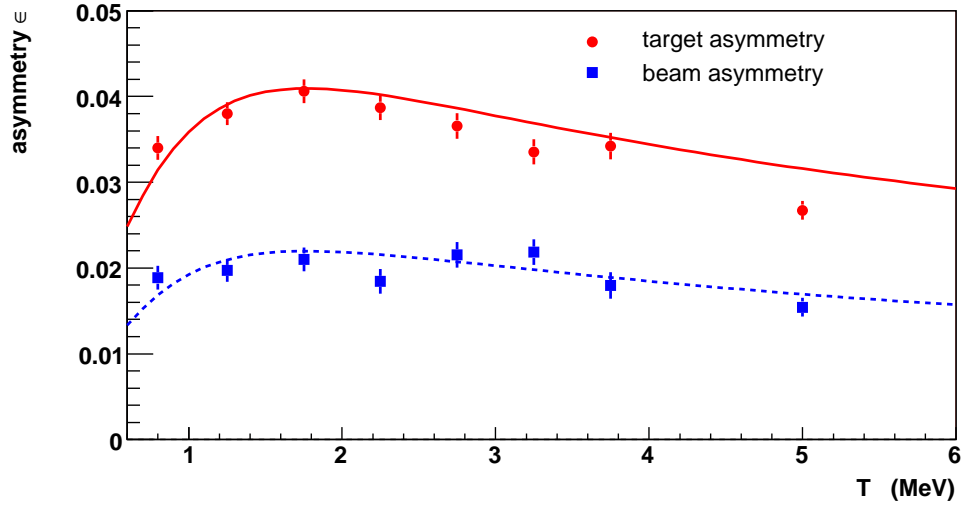
Figure 27: Square root asymmetries for data set 5 (blue beam, *120-bunch mode*) as functions of recoil energy T_R.

Figure 28: Background contributions to asymmetries and asymmetry ratios for data set 3, see text for details about the symbols in the left figure.
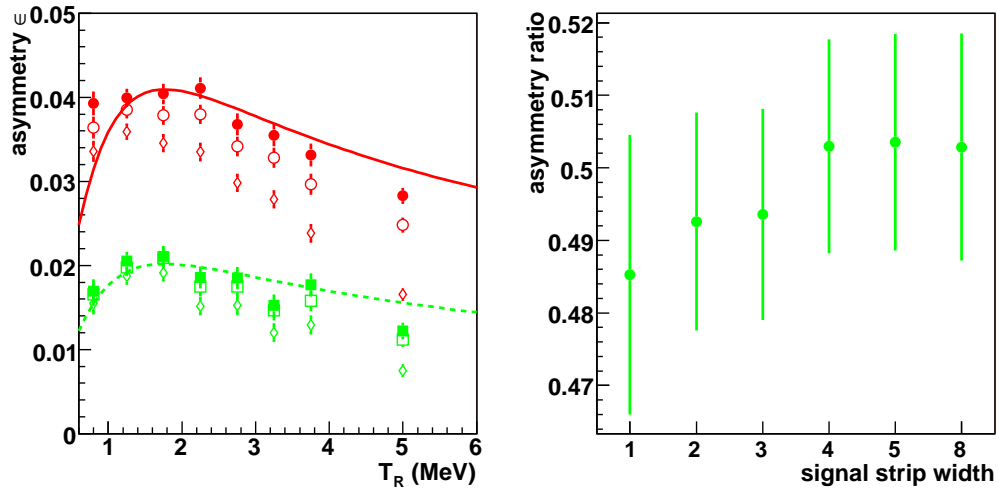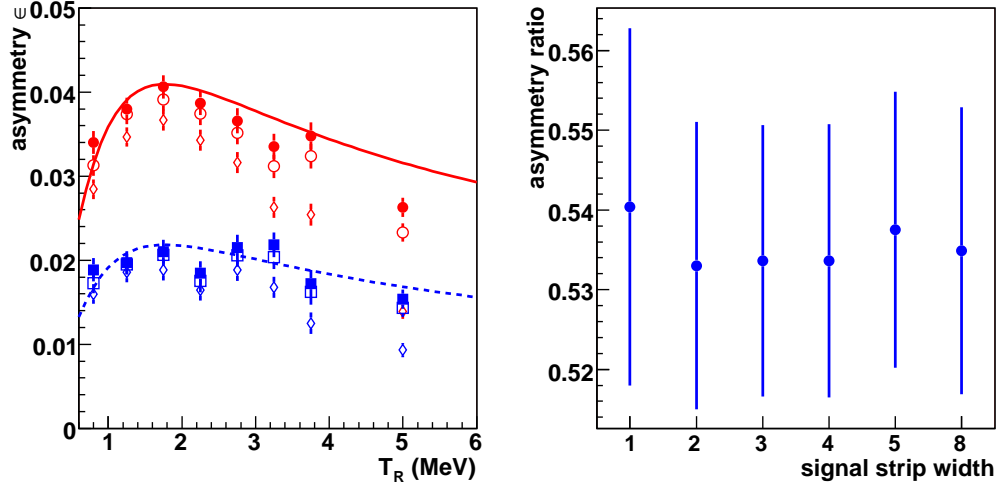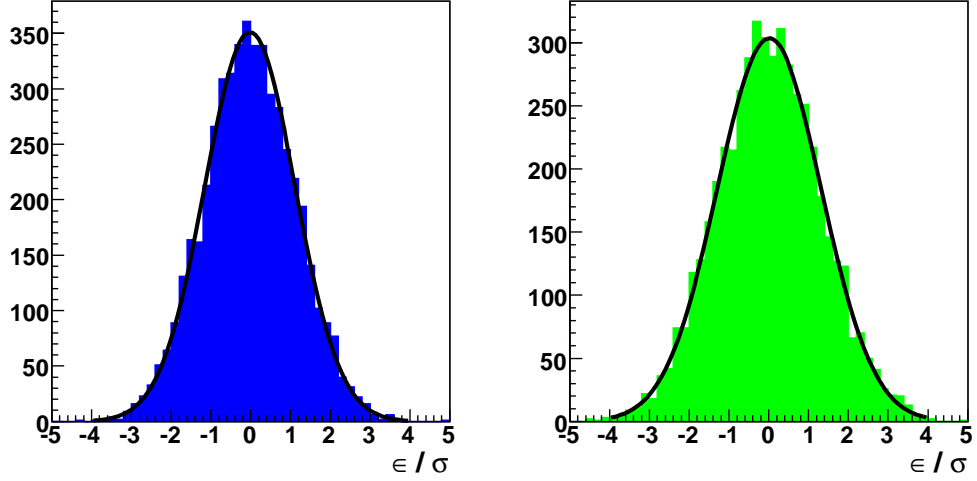
48

Figure 29: Background contributions to asymmetries and asymmetry ratios for data set 5, see text for details about the symbols in the left figure.

Figure 30: Bunch shuffling results (5000 repetitions) for data set 3. Asymmetries have been scaled with statistical errors to make deviations from the expected shape more distinctive.
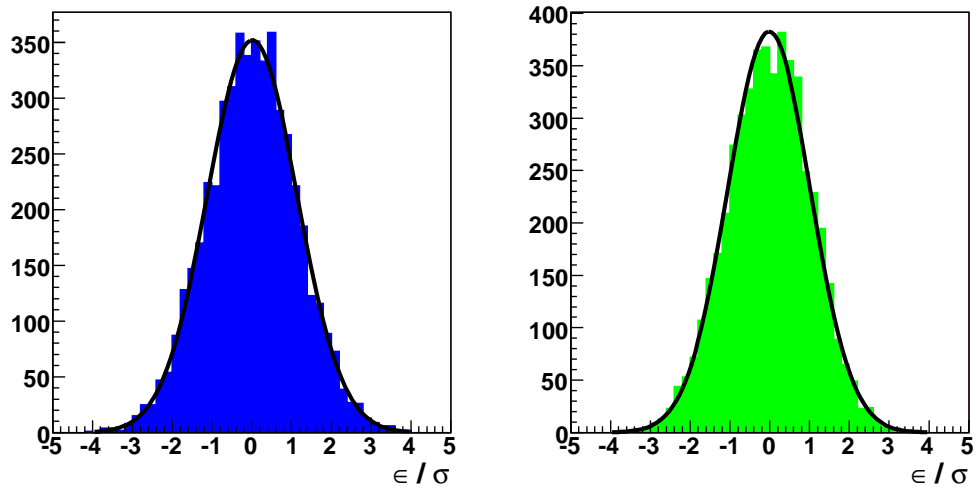
49

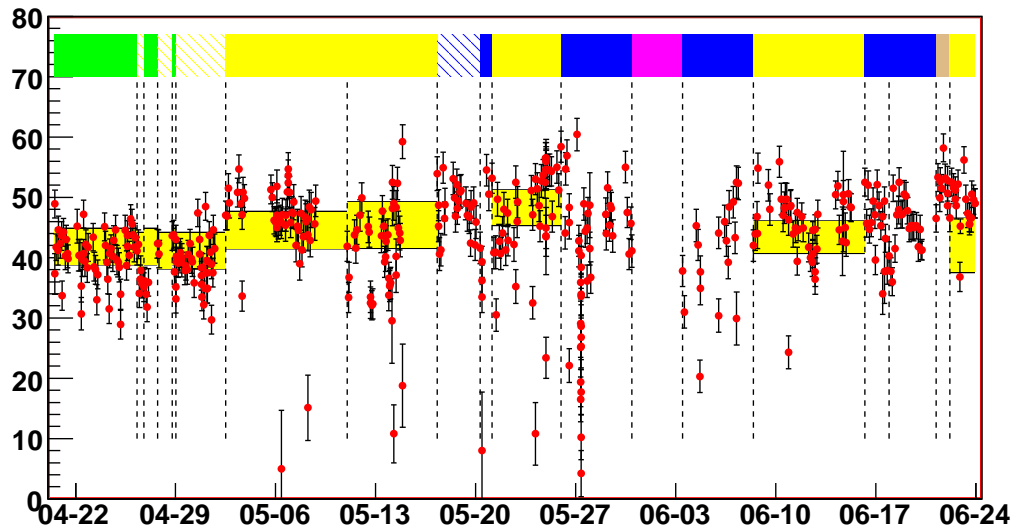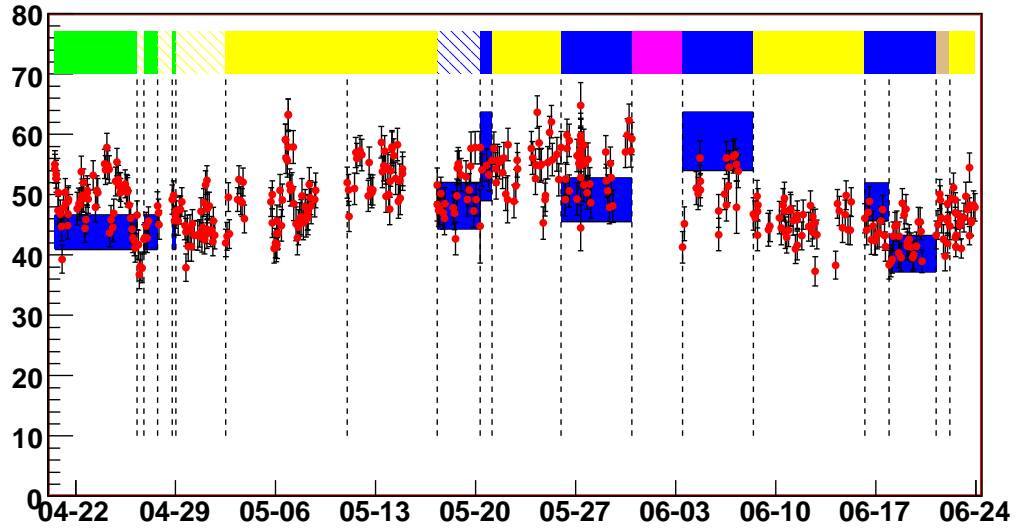Figure 31: Bunch shuffling results (5000 repetitions) for data set 5.

Figure 32: Comparison of results of the jet polarimeter (colored boxes) with the pC-polarimeter online numbers (red circles) (top: blue beam polarizations, bottom: yellow beam polarizations). The vertical dashed lines indicate a change of the jet polarimeter setup. Detailed explanation of color codes in the text.

51

References

[1] H. Okada et al., Phys. Lett. B638, 450 (2006).

[2] A. Zelinski et al., Nucl. Instr. Meth. A536, 248 (2005); T. Wise et al., Nucl. Instr. Meth. A559, 1 (2006).

[3] H. Okada, Doctor of Science Thesis, Kyoto University (2006).

[4] M.J. Berger et al., http://physics.nist.gov/ PhysicsRef-Data/Star/Text/contents.html

[5] G.G. Ohlsen and P.W. Keaton *Techniques for measurement of spin-$\frac{1}{2}$ and spin-1 polarization analyzing tensors.* Nucl. Instr. and Meth. **109** (1973), 41.

[6] I. Nakagawa et al., CNIpol analysis note for 2005, CAD Note 275.